Routes to chaos in the Hopf-saddle-node bifurcation for fixed points of 3D-diffeomorphisms

Vitolo, Renato; Broer, Henk; Simo, Carles

Published in:
Nonlinearity

DOI:
10.1088/0951-7715/23/8/007

Publication date:
2010

IOP PUBLISHING NONLINEARITY

Nonlinearity **23** (2010) 1919–1947 doi:10.1088/0951-7715/23/8/007

Routes to chaos in the Hopf-saddle-node bifurcation for fixed points of 3D-diffeomorphisms*

Renato Vitolo[1,4,5], **Henk Broer**[2] **and Carles Simó**[3]

[1] School of Engineering, Computing and Mathematics, University of Exeter, Exeter, UK
[2] Johann Bernoulli Institute for Mathematics and Computer Science, PO Box 407, 9700 AK Groningen, The Netherlands
[3] Deptartament de Matemàtica Aplicada i Anàlisi, Universitat de Barcelona, Gran Via 585, 08007 Barcelona, Spain

E-mail: r.vitolo@exeter.ac.uk

Received 29 December 2009, in final form 15 April 2010
Published 5 July 2010
Online at stacks.iop.org/Non/23/1919

Recommended by L-S Young

Abstract

Dynamical phenomena are studied near a Hopf-saddle-node bifurcation of fixed points of 3D-diffeomorphisms. The interest lies in the neighbourhood of weak resonances of the complex conjugate eigenvalues. The 1 : 5 case is chosen here because it has the lowest order among the weak resonances, and therefore it is likely to have a most visible influence on the bifurcation diagram. A model map is obtained by a natural construction, through perturbation of the flow of a Poincaré–Takens normal form vector field. Global bifurcations arise in connection with a pair of saddle-focus fixed points: homoclinic tangencies occur near a sphere-like heteroclinic structure formed by the 2D stable and unstable manifolds of the saddle points. Strange attractors occur for nearby parameter values and three routes are described. One route involves a sequence of quasi-periodic period doublings of an invariant circle where loss of reducibility also takes place during the process. A second route involves intermittency due to a quasi-periodic saddle-node bifurcation of an invariant circle. Finally a route involving heteroclinic phenomena is discussed. Multistability occurs in several parameter subdomains: we analyse the structure of the basins for a case of coexistence of a strange and a quasi-periodic attractor and for coexistence of two strange attractors. By construction, the phenomenology of the model map is expected in generic families of 3D diffeomorphisms.

Mathematics Subject Classification: 37G10, 34C37, 37D45

(Some figures in this article are in colour only in the electronic version)

* In memoriam: Floris Takens.
[4] Please contact the corresponding author (R Vitolo) for high-resolution versions of the figures.
[5] Postal address: Dr Renato Vitolo, College of Engineering, Mathematics and Physical Sciences, University of Exeter, Harrison Building, room 273, North Park Road, Exeter, EX4 4QF, UK.

1. Introduction

The Hopf-saddle-node (HSN) bifurcation for fixed points of 3D diffeomorphisms occurs when the eigenvalues of the derivative at the fixed point are,

$$e^{i\omega_0},\ e^{-i\omega_0} \text{ and } 1, \tag{1}$$

subject to the non-resonance conditions

$$e^{in\omega_0} \neq 1 \qquad \text{for } n = 1, 2, 3, 4, \tag{2}$$

and to generic requirements on the higher-order terms and on the parameter dependence [14, lemma 6]. HSN bifurcations of fixed points have been found as organizing centres for the bifurcation diagrams of

(1) a 3D atmospheric model subject to a slow periodic parametric forcing [12, 23], describing the atmospheric baroclinic jet at midlatitudes in the Northern Hemisphere;
(2) a 48D autonomous atmospheric model used to study the phenomenon of low-frequency variability [50].

Strange attractors were found near these HSN bifurcations, related to the breakdown of invariant circles for suitable return maps: the global Poincaré map for model 1 and a local Poincaré map near a periodic orbit for model 2. This paper aims to analyse the mechanisms leading to the creation of strange attractors in such HSN bifurcations.

We consider a model map which is 'as generic as possible' in the class of diffeomorphisms having a HSN bifurcation near a weak resonance [14]. The model map is constructed by perturbing the flow of a truncated normal form for the HSN bifurcation for *vector fields*. The advantage of this approach is to provide direct control on the location of relevant phenomena in the parameter space of the model. We expect the rich phenomenology of the model to occur in generic families of 3D diffeomorphisms. Our expectation is based on a modified version of Takens's theorem [51], stating that any HSN family of diffeomorphisms can be approximated by the time-one map of a HSN family of vector fields [14, theorem 1].

1.1. Setting of the problem

For a HSN bifurcation of equilibria of vector fields, the eigenvalues are $\pm i\omega$ and 0 (logarithms of (1)) at the central singularity. This linear part induces a formal axial symmetry [3, 20, 52] which allows a good approximation by a family of axially symmetric vector fields near the central singularity in the product of phase space and parameter space, see [40, lemma 8.11]. In cylindrical coordinates (r, ϕ, z), the planar vector field

$$\dot{r} = r(-\beta_2 - a_1 z - z^2), \qquad \dot{z} = -\beta_1 - z^2 - sr^2 \tag{3}$$

is obtained by discarding the angular dynamics $\dot{\phi}$ around the symmetry axis z. Here $a_1 \in \mathbb{R}$ and $s = \pm 1$ are constants and $\beta_j \in \mathbb{R}$ are parameters. The richest bifurcation diagram occurs for the unfolding case $a_1 < 0$, $s = 1$, see figure 1. A sphere-like heteroclinic connection occurs for the corresponding 3D vector field, for parameters on the curve $\mathcal{HET}$. In generic perturbations of this truncated normal form, the heteroclinic sphere splits into a transversal heteroclinic structure, allowing for the occurrence of Shil′nikov homoclinic bifurcations [21, 30, 31, 40, 45, 46]. Our main question is as follows: *what are the bifurcation patterns for HSN diffeomorphisms corresponding to these homoclinic and heteroclinic bifurcations?* We attack this problem by studying the model map

$$G : \begin{pmatrix} w \\ z \end{pmatrix} \mapsto \begin{pmatrix} e^{i(\omega_0+\gamma\delta)} w[1 - \gamma(\gamma\mu + az + \gamma z^2)] \\ z + \gamma(1 - |w|^2 - z^2) \end{pmatrix} + \begin{pmatrix} \gamma^3(\varepsilon_1 \bar{w}^4 + \varepsilon_2 z^4) \\ 0 \end{pmatrix}, \tag{4}$$

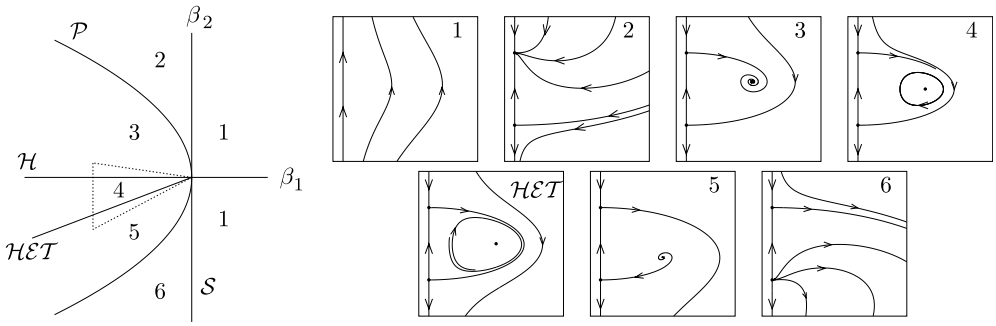

Figure 1. Bifurcation diagram and phase portraits of (3) for $s = 1$, $a_1 < 0$ [40, section 8.5]. Hopf and heteroclinic bifurcations are denoted as $\mathcal{H}$ and $\mathcal{HET}$, respectively.

with $w = x + \mathrm{i}y \in \mathbb{C}$, $z \in \mathbb{R}$ and $a = a_1 + \mathrm{i}a_2 \in \mathbb{C}$. As in [14] we fix $\varepsilon_1 = \varepsilon_2 = 1$, $a_1 = -1$, $a_2 = 1/\sqrt{2}$: our choice for the coefficients is discussed in [57, appendix 4E]. Other values have been tested and no relevant qualitative differences were observed. Map (4) therefore depends on the real parameters (γ, μ, δ), where δ is a small detuning near the $1:5$ resonance $\omega_0 = 2\pi/5$. This resonance is selected, because it has the lowest order compatible with (2): it is therefore expected to have the most visible influence on the bifurcation diagram, amongst all weak resonances. The construction of our model map is briefly sketched here, see [14, 15] and [57, section 4.1.2] for details. Defining $w = r\mathrm{e}^{\mathrm{i}\phi}$, the 3D vector field

$$\dot{w} = (-\beta_2 + \mathrm{i}\omega)w - awz - wz^2, \qquad \dot{z} = -\beta_1 - sw\bar{w} - z^2 \tag{5}$$

is obtained by reintroducing the angular dynamics $\dot{\phi}$ in (3). We focus on the parameter region where Hopf and heteroclinic bifurcations occur (dashed triangle in the halfplane $\beta_1 < 0$, figure 1). The following transformation of time and variables is applied:

$$\beta_1 = -\gamma^2, \quad \beta_2 = \gamma^2\mu, \quad t = \widehat{t}/\gamma, \quad w = \gamma\hat{w}, \quad z = \gamma\hat{z}. \tag{6}$$

The first term in (4) is an approximate time-γ map of the vector field (5) after transformation (6), with hats removed for simplicity. To obtain the approximation the rotational part is included in the $\mathrm{e}^{\mathrm{i}(\omega_0+\gamma\delta)}$ factor, while the flow of (5) is approximated by Euler's method. The second term of (4) consists of perturbative terms of order four, one of them resonant. By [14, theorem 1], this construction contains a subclass of generic phenomena for HSN diffeomorphisms.

1.2. A roadmap in the parameter space

The qualitative sketch in figure 2 summarizes our expectations for the bifurcation diagram of model map G and serves as reference in our study. Map G can be seen as a perturbation of the time-1 map of the 3D vector field (5): the latter map is an axially symmetric 3D diffeomorphism. Figure 2(a) sketches the bifurcation diagram of this diffeomorphism in the parameter space (γ, μ, ω). We focus on the transition from region 3 to 4 in figure 2(a) (equivalently, from region 3 to 4 in figure 1).

The equilibrium off the z-axis in the phase portraits of figure 1 corresponds to an invariant circle attractor for the time-1 map of (5). This circle attractor will be denoted as $\mathscr{C}$ for the rest of this section. When μ decreases across zero the circle attractor $\mathscr{C}$ loses stability and an invariant 2-torus branches off. For parameters on $\mathcal{HET}$ the 2-torus merges with an invariant sphere formed by the invariant manifolds of two fixed points $P_\pm$ of saddle-focus type. These points correspond to the equilibria on the z-axis in figure 1. Due to the scaling (6), $P_\pm$ are

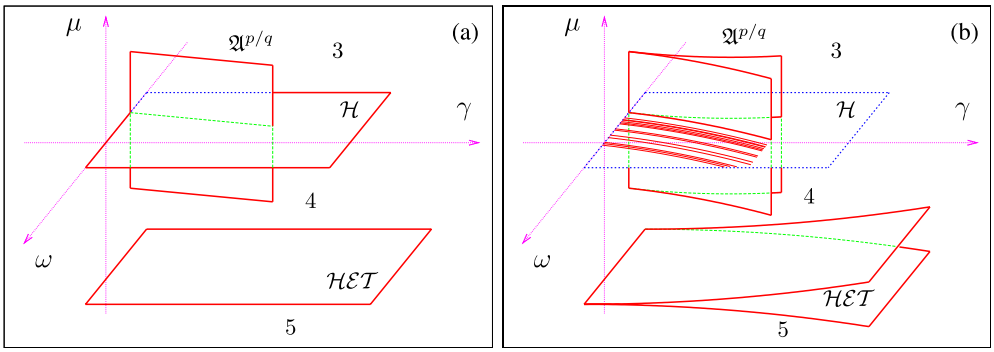

Figure 2. Theoretical expectations for the bifurcation diagram of model map G (4) in the parameter space (γ, μ, ω). (a) Bifurcation set for the time-1 map of the vector field (5). Parameter values for which the rotation number on the invariant circle $\mathscr{C}$ is a fixed rational number $p/q \in \mathbb{Q}$ form a hypersurface $\mathfrak{A}^{p/q}$. (b) Expected bifurcation set of G: the invariant circle $\mathscr{C}$ has rotation number p/q for parameters in a resonance wedge $\mathfrak{A}^{p/q}$; transversal heteroclinic intersections and tangencies occur in a wedge $\mathcal{HET}$. Quasi-periodic Hopf bifurcations occur on a frayed boundary $\mathcal{H}$ given by a Cantor-like foliation by curves where the rotation number of $\mathscr{C}$ is Diophantine. See [14, 15] for details.

approximately located at the 'poles' $\approx (0, 0, \pm 1)$. Note that for the map (4), even with $\varepsilon_1 = \varepsilon_2 = 0$ the invariant sphere is destroyed and separatrix splitting occurs.

Figure 2(b) shows the structure of the parameter space for G, deduced from figure 2(a) on the basis of perturbation theory, normal hyperbolicity and quasi-periodic bifurcation theory [2, 4–9, 19, 28, 29, 34]. A normally hyperbolic invariant circle $\mathscr{C}$ still persists for μ away from zero. However, the dynamics on the circle is resonant for parameter values inside resonance wedges. Quasi-periodic Hopf bifurcations occur for parameters on a frayed boundary $\mathcal{H}$. This frayed boundary consists of a Cantor set of curves contained inside a surface, the gaps of which are filled up with resonance 'bubbles', see appendix A.

The parameter γ will be fixed to 0.1 for the rest of this paper. This amounts to restrict to a vertical plane in figure 2(b), parametrized by (μ, δ). The choice $\gamma = 0.1$ is discussed in [14] and [57, appendix 4E]. This value is small enough to be close to the bifurcation and large enough to be able to detect numerically most of the relevant phenomena.

Remark 1: Shift of the Hopf and heteroclinic bifurcations. As proved in [14, lemma 2], the Hopf bifurcation occurs for $\mu \to 1$ as $\gamma \to 0$ for map (4), while it occurs for $\mu \to 0$ as $\gamma \to 0$ for vector field (3) (with the scaling (6)). Similarly, the location of $\mathcal{HET}$ moves from a negative value of μ for (3) to a positive value for (4) as $\gamma \to 0$, all other parameters being kept fixed at the selected values.

Figure 3 shows the bifurcation diagram of G in this (μ, δ)-parameter plane. The diagram is computed by means of Lyapunov exponents, see [14, 57] for details. To interpret figure 3 we recall that, by (6), to decrease μ is roughly equivalent to decrease β_2 in figure 1.

(1) A circle attractor $\mathscr{C}$ occurs for large μ and is $1:5$-resonant within the strip pointed by an arrow in figure 3. This strip corresponds to the intersection of the wedge $\mathfrak{A}^{p/q}$ in figure 2(b) (for $p/q = 1/5$), with the vertical plane $\{\gamma = 0.1\}$. The circle $\mathscr{C}$ undergoes a quasi-periodic Hopf bifurcation near $\mu = 0.97$. This frayed boundary corresponds to the intersection of the Cantor-like set $\mathcal{H}$ (see figure 2(b)) with the plane $\{\gamma = 0.1\}$ (for simplicity, this intersection is denoted as $\mathcal{H}$ as well). An intricate bifurcation structure occurs at the intersection of the $1:5$ resonance strip with $\mathcal{H}$: this is the main topic of [14].

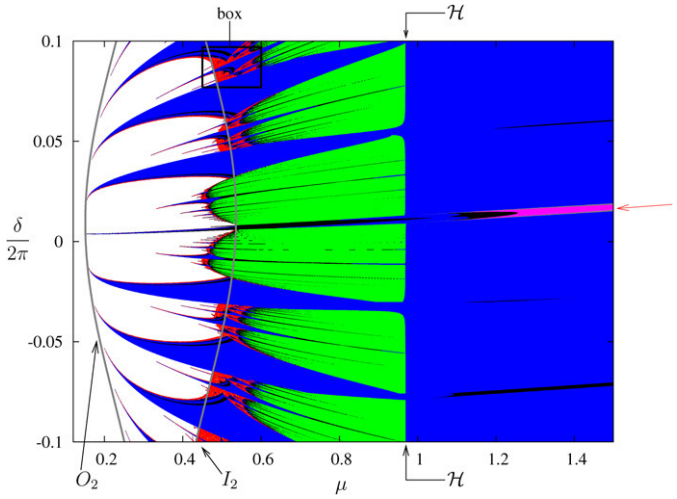

Figure 3. Lyapunov diagram of model map G (see (4)). Parameters are scanned on a regular grid, decreasing μ along lines of constant δ. For each (μ, δ), the detected attractor is classified according to its Lyapunov exponents: see [14, 15, 49, 57] for the algorithm and table 1 for the colour code. Yellow and pale blue pixels are very rare, grey regions occur near the boundary of the 1 : 5 resonance gap pointed to by an arrow. Quasi-periodic Hopf bifurcations take place on a frayed boundary $\mathcal{H}$ near $\mu = 0.97$, from which several resonance tongues emerge towards the left.

(2) A 2-torus attractor $\mathscr{T}_-$ branches off from the circle $\mathscr{C}$ at the quasi-periodic Hopf bifurcation $\mathcal{H}$. Two types of resonance can take place either independently or simultaneously in the 2-torus attractors. Generically this gives rise to a dense set of resonance tongues in the parameter plane. This structure is studied in [15].

(3) The region between the curves I_2 and O_2 in figure 3 corresponds to region $\mathcal{HET} \cap \{\gamma = 0.1\}$ in figure 2(*b*) and it is denoted as $\mathcal{HET}$ for simplicity. This region is characterized by the occurrence of heteroclinic intersections of the 2D manifolds $W^s(P_-)$ and $W^u(P_+)$, where $P_\pm$ are the 'polar' saddle-focus fixed points. Figure 5 shows the configuration of the invariant manifolds of $P_\pm$ just before entering region $\mathcal{HET}$, where the 2-torus attractor still exists. The 2-torus is destroyed between curves I_2 and O_2 and strange attractors are created through various routes. These phenomena are the focus of this paper.

1.3. Strange attractors and routes to chaos

Figures 3 and 4 show that strange attractors of G mostly occur in region $\mathcal{HET}$, and particularly near curve I_2. We call an attractor *strange* and the corresponding dynamics *chaotic* if the maximal Lyapunov exponent ℓ_1. We identify two classes of strange attractors by the Lyapunov exponents $\ell_1 \geqslant \ell_2 \geqslant \ell_3$, see table 1:

$\ell_1 > 0, \ell_2 < 0$ (yellow in figure 3): these will be called *Hénon-like*.
$\ell_1 > 0, \ell_2 \approx 0$ (red): these will be called *quasi-periodic Hénon-like*.

Hénon-like strange attractors coincide with the closure of the 1D unstable manifold of a periodic orbit of saddle type [1, 42, 43, 54, 56] and possess one direction of instability [59], while the remaining directions are contracting. Quasi-periodic Hénon-like strange attractors coincide with the closure of the unstable manifold of a quasi-periodic invariant circle of saddle

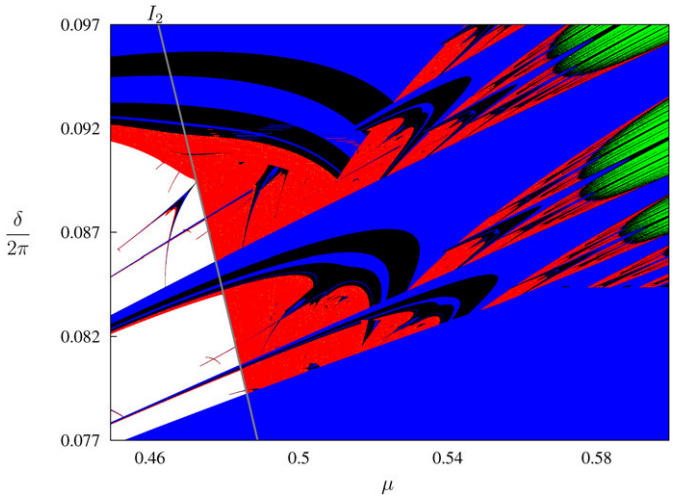

Figure 4. Magnification of the box highlighted in figure 3, showing the 'tails' of several resonance tongues emanating from the frayed boundary $\mathcal{H}$. The 'broken' boundaries of several domains give good evidence of multiplicity of attractors.

Table 1. Colour coding for the Lyapunov diagrams in figures 3, 4. The attractors of model map G (4) are classified by means of the Lyapunov exponents (ℓ_1, ℓ_2, ℓ_3).

Colour	Lyapunov exponents	Attractor type
Red	$\ell_1 > 0 = \ell_2 > \ell_3$	Strange attractor
Yellow	$\ell_1 > 0 > \ell_2 > \ell_3$	Strange attractor
Blue	$\ell_1 = 0 > \ell_2 = \ell_3$	Invariant circle of focus type
Green	$\ell_1 = \ell_2 = 0 > \ell_3$	Invariant 2-torus
Black	$\ell_1 = 0 > \ell_2 > \ell_3$	Invariant circle of node type
Grey	$0 > \ell_1 > \ell_2 = \ell_3$	Fixed point of focus type
Fuchsia	$0 > \ell_1 = \ell_2 \geqslant \ell_3$	Fixed point of focus type
Pale blue	$0 > \ell_1 > \ell_2 > \ell_3$	Fixed point of node type
White		No attractor detected

type [12, 13, 16, 57]. Parameter regions with Hénon-like strange attractors are expected to be nowhere dense sets of positive measure [1, 42].

Remark 2: Classifying attractors. Throughout this paper, we will use numerical evidence to classify the attractors (e.g. Hénon-like versus quasi-periodic Hénon-like). For example, the classification in table 1 relies on the numerical computation of the Lyapunov exponents. Other numerical indicators, such as the rotation vector (appendix B.5), will be used later on for this purpose. Although these methods do not provide a proof of existence, it gives a coherent indication on the nature of the underlying attractor.

The parameter regions characterized by strange attractors mostly surround the 'tail' of the resonance tongues emerging from the quasi-periodic Hopf boundary $\mathcal{H}$ (figures 3 and 4). An invariant circle attractor exists for parameters inside a tongue: the circle may be of focus or node type in the normal direction (see table 1). Most tongues widen up and eventually overlap for small μ, as can be deduced from figure 4. Overlapping of resonance tongues with other tongues yields coexistence of different invariant circles for the same parameter values.

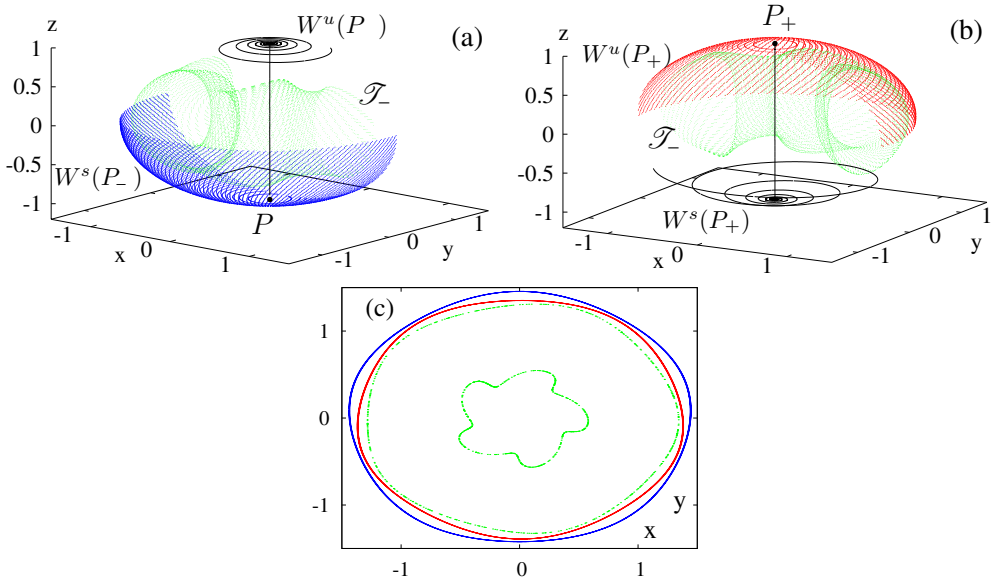

Figure 5. (*a*) Invariant 2-torus attractor $\mathscr{T}_-$ of the diffeomorphism G (4) with the saddle-focus fixed point P_- and portions of the manifolds $W^s(P_-)$ and $W^u(P_-)$, which are 2D and 1D, respectively. Only points with $y < 0$ ($y < 0.2$) are shown for $\mathscr{T}_-$ (respectively, $W^s(P_-)$). (*b*) $\mathscr{T}_-$ with the saddle-focus fixed point P_+ and portions of the manifolds $W^u(P_+)$ and $W^s(P_-)$, which are 2D and 1D, respectively. Only points with $y > 0$ ($y > -0.3$) are shown for $\mathscr{T}_-$ (respectively, $W^u(P_+)$). (*c*) Equatorial intersections of the 2D manifolds $W^s(P_-)$ and $W^u(P_+)$ with the plane $z = 0$, with a 'slice' of the attractors $\mathscr{T}_-$ by a layer of width 2×10^{-5} around the plane $z = 0$.

We analyse three routes to chaos. The first two routes start for parameters in the interior of a resonance tongue and involve exiting the tongue across its 'tail' through a sequence of quasi-periodic period doublings (section 2) or its 'sides' through a quasi-periodic saddle-node bifurcation (section 3). The third route is related to the heteroclinic tangencies of the saddle-focus fixed points $P_\pm$ (section 4). This leads to coexistence of an invariant circle attractor with a strange attractor or coexistence of two strange attractors in certain parameter regions and we study the structure of the basins of attraction in relation to the invariant manifolds of $P_\pm$. Open problems are summarized in section 5.

Remark 3: Novelty of our approach. The quasi-periodic period doubling route has been already described [12, 16, 55], but we provide a more detailed analysis. The saddle-node route is a novel phenomenon. To our best knowledge, none of these routes has been put in relation to the HSN bifurcation for fixed points of diffeomorphisms. Also, the occurrence of these routes and the coexistence of attractors near the heteroclinic tangencies cannot be predicted from normal form analysis.

2. The quasi-periodic period doubling route

This is a typical route for the creation of quasi-periodic strange attractors [16]. It occurs in many systems involving oscillatory instabilities, such as (geophysical) fluid dynamical models [12, 41, 55, 57]. Despite recent progress [32, 33, 38], the main theoretical questions (existence of strange attractors and finiteness of the doubling sequence) remain unanswered.

Sequences of quasi-periodic period doublings of an invariant circle [4, 5, 9] occur at the 'tail' of most resonance tongues in figure 4. The sequences are identified by the alternating strips where an invariant circle of node/focus type occurs, preceding the parameter regions with strange attractors (see table 1). Do *finitely* or *infinitely* many quasi-periodic doublings precede the creation of a strange attractor?

The numerical evidence we have collected suggests that finitely many doublings take place and we propose the following explanation. The invariant circle attractors lose reducibility at some moment between two consecutive doublings (see appendix A for the meaning of reducibility). Then a strange attractor is formed *at once*, when the maximal Lyapunov exponent vanishes for a non-reducible invariant circle. This scenario is based on [32, 33], where a linear version of the problem is studied, on [38], where a 1D example is worked out, and on [10], which discusses several consequences of the lack of reducibility in linear problems. The existence of a strange attractor is conjectural here as well as in all the above references.

Remark 4: Quasi-periodic period doublings and resonance 'bubbles'. We shall describe this route by examining the evolution of invariant circle attractors as the parameter μ is varied. Our detection of quasi-periodic bifurcations relies on monitoring the μ-values where the second Lyapunov exponent ℓ_2 vanishes. As we explain in appendix A, we cannot ensure that the dynamics is quasi-periodic *exactly* at the μ-values where ℓ_2 vanishes, due to the unavoidable occurrence of resonance on the invariant circles. For this reason, we can only say that a quasi-periodic bifurcation is expected *for nearby* (μ, δ)-parameter values. In the example below we find, however, that the resonances of the invariant circles occupy a parameter set of very small measure. The problem of resonances is avoided when studying skew-product families with an irrational rotation [32, 33, 38].

This route starts from an invariant circle attractor $\mathscr{L}_0$ (figure 6(*A*)), for parameters inside a resonance tongue. Five consecutive quasi-periodic period doublings take place as μ is decreased, where 'doubled' circle attractors $\mathscr{L}_1, \ldots, \mathscr{L}_5$ are created ($\mathscr{L}_2$ is shown in figure 6(*B*)). These bifurcations are of 'length doubling' type: the 'doubled' circle attractor $\mathscr{L}_{i+1}$ is one connected closed curve and its length is roughly twice the length of the circle $\mathscr{L}_i$ which has lost stability [5, 12, 22], also see appendix A.

A strange attractor replaces $\mathscr{L}_5$ by decreasing μ (figure 7(*A*)). This ribbon-shaped strange attractor is formed by the union of a finite number of narrow *bands*, closely winding around the phase-space region previously occupied by $\mathscr{L}_5$. The multiple bands merge together as μ decreases (figure 7(*B*)). A similar band-merging process has been described for the Hénon-Pomeau attractor in [47].

This is illustrated by 'slicing' the attractors, that is selecting points within thin horizontal layers. The circle attractors in figure 6(*A*) and (*B*) intersect the plane $z = 0$ at 10 and 40 points, respectively. The strange attractor in figure 7(*A*) occurs after the breakdown of the invariant circle attractors and has a four-banded structure. The four bands merge into a single band for the attractor in figure 7(*B*). The banded structures are visualized in the 'equatorial slices' magnified in the boxes of figure 6. A similar merging process has been observed in [44] for a model of thermal convection in binary fluid mixtures, using discretizations ranging from 3×2^{10} to 3×2^{12} modes.

The second Lyapunov exponent of the strange attractors in figure 7(*A*) and (*B*) equals zero within the achieved numerical precision. All the above suggest that these strange attractors are of quasi-periodic Hénon-like type, see section 1.3. In particular, the single-band attractor in figure 7(*B*) might coincide with the closure of $W^u(\mathscr{L}_0)$. We plan to investigate this possibility in simpler models, such as that of [13].

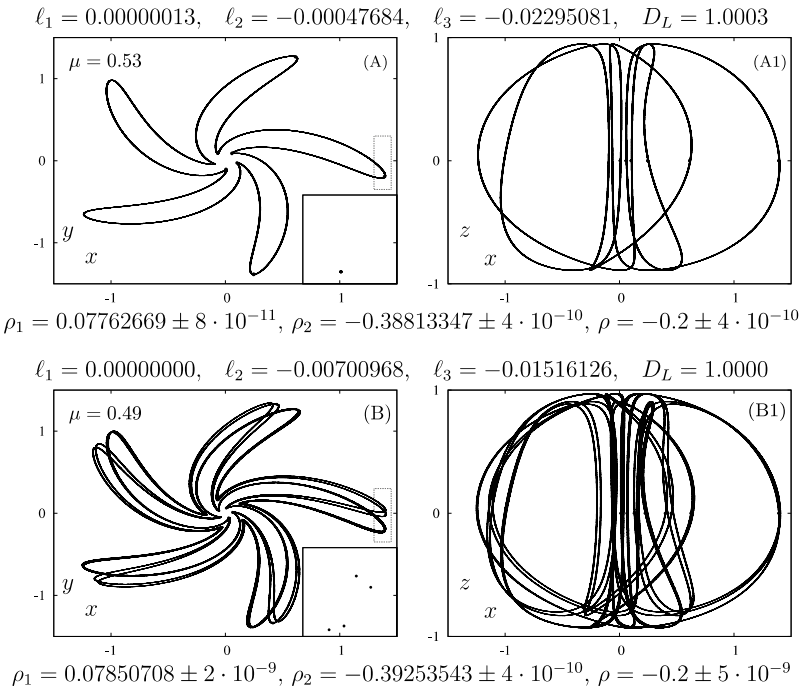

Figure 6. Quasi-periodic invariant circle attractors of the model map G (4) for $\delta/(2\pi) = 0.0324$. Top row: $\mu = 0.53$, projection on the (x, y)-plane (A) and the (x, z)-plane $(A1)$. Bottom row: $\mu = 0.49$, projection on the (x, y)-plane (B) and (x, z)-plane (B1). The boxes in the left column magnify 'slices' of the attractors by a layer of width $2 \cdot 10^{-5}$ around the plane $z = 0$, in the window $(x, y) \in [1.382, 1.408] \times [-0.25, 0.17]$. Points of the slices with $x > 0$ are added as thick dots to (A) and (B). The dynamics on these attractors is classified on the basis of numerical evidence, see remark 2. Lyapunov exponents ℓ_j and dimension D_L are given at the top of each plot. Rotation numbers ρ_j and uncertainties σ_{ρ_j}, for $j = 1, 2$ are given below each plot together with ratio $\rho = \rho_1/\rho_2$ and related uncertainty σ_ρ.

The lack-of-reducibility scenario is suggested by the evolution of the Lyapunov exponents $\ell_1 \geqslant \ell_2 \geqslant \ell_3$ as μ is varied with fixed δ. Quasi-periodic period doublings occur near (see remark 4) the parameter values where ℓ_2 vanishes (μ_1 to μ_5 in figure 8). The doubled circle attractor $\mathscr{L}_1$ is formed as μ decreases across μ_1, where $\mathscr{L}_0$ loses stability. Near the bifurcation, both circles are reducible and of node type in the normal direction: this explains the alternating node/focus strips within the resonance tongues in figure 4.

At the second doubling (across μ_2), one of the normal eigenvalues of $\mathscr{L}_1$ crosses -1. There exists an interval between μ_2 and μ_1 (labelled by C_1 in figure 8(a)) where the two normal eigenvalues are complex: this is where $\ell_2 = \ell_3$. A narrower such interval, labelled by C_2, occurs near $\mu = 0.49$. This process is typical for periodic points of diffeomorphisms and is described in, e.g., [11, figure 12]. Loosely speaking, the normal eigenvalues of $\mathscr{L}_1$ first 'collide', leaving the positive real axis to enter the complex plane, then race around the origin and collide again on the negative real axis. This is the only way in which one eigenvalue can cross -1, starting from the real positive axis. For this to be possible, however, the invariant circle must be reducible [37].

The above process breaks down for smaller μ: $\mathscr{L}_3$ and $\mathscr{L}_4$ *never become of focus type*. As μ is decreased, $\mathscr{L}_3$ crosses a parameter region N_1 where it ceases to be reducible: $\mathscr{L}_3$ is reducible at the right of region N_1, where the eigenvalues are real and positive, whereas the

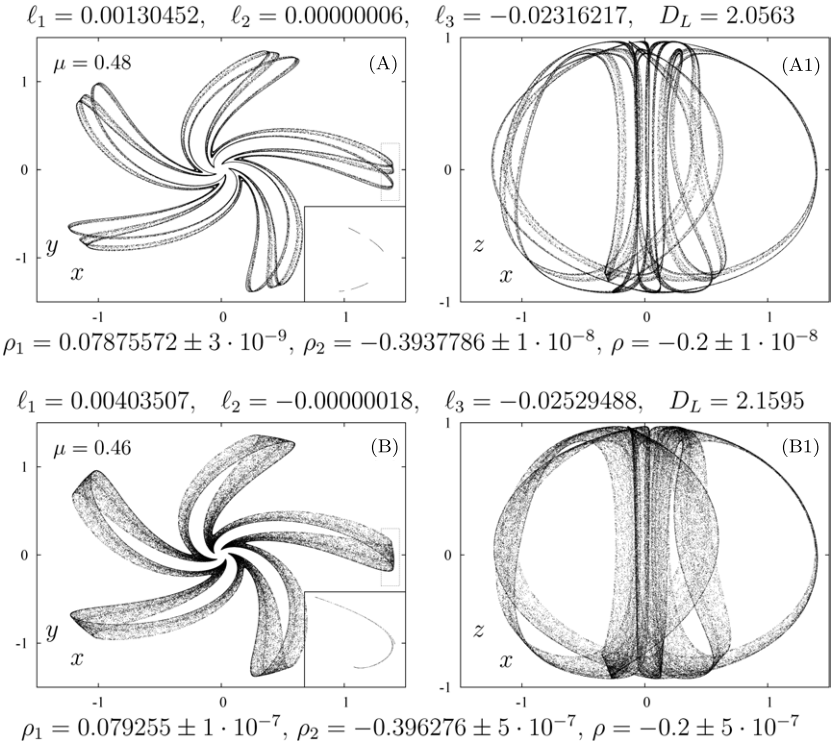

Figure 7. Quasi-periodic Hénon-like strange attractors of the model map G (4) for $\delta/(2\pi) = 0.0324$. Top row: $\mu = 0.48$, projection on the (x, y)-plane (A) and the (x, z)-plane $(A1)$. Bottom row: $\mu = 0.46$, projection on the (x, y)-plane (B) and (x, z)-plane (B1). The boxes in the left column magnify 'slices' of the attractors by a layer of width 2×10^{-5} around the plane $z = 0$, in the window $(x, y) \in [1.382, 1.408] \times [-0.25, 0.17]$. The 'slices' in (A) and (B) display a four-piece and a single-piece Hénon-like structure respectively, compare with, e.g., [11]. The dynamics on these attractors is classified on the basis of numerical evidence, see remark 2. Lyapunov exponents ℓ_j and dimension D_L are given at the top of each plot. Rotation numbers ρ_j and uncertainties σ_{ρ_j}, for $j = 1, 2$ are given below each plot together with ratio $\rho = \rho_1/\rho_2$ and related uncertainty σ_ρ.

eigenvalues are real and negative at the left of N_1 (figure 8(b)). The fact that $\ell_2 \neq \ell_3$ for $\mu \in N_1$ is not an artefact due to the coarse resolution of figure 8(a), as illustrated by the magnifications in the boxes of figure 8(b).

Lack of reducibility occurs in increasingly larger parameter sets for $\mathscr{L}_4$ and $\mathscr{L}_5$. Figure 8(c) suggests that a strange attractor appears at once when $\mathscr{L}_5$ undergoes a quasi-periodic doubling, where the second Lyapunov exponent vanishes: we conjecture that $\mathscr{L}_5$ is not reducible at that moment. The analysis is complicated here by the unavoidable occurrence of resonances for the dynamics on the invariant circles as the parameter μ is varied, see appendix A.

3. The intermittency route

This route is a novel phenomenon, to the best of our knowledge. It may be expected in systems of ordinary differential equations with an invariant three-torus, since this would correspond to a 2-torus for a Poincaré map. This route amounts to exit one of the resonance tongues in figure 4 across its 'sides', straight into the parameter region where strange attractors occur.

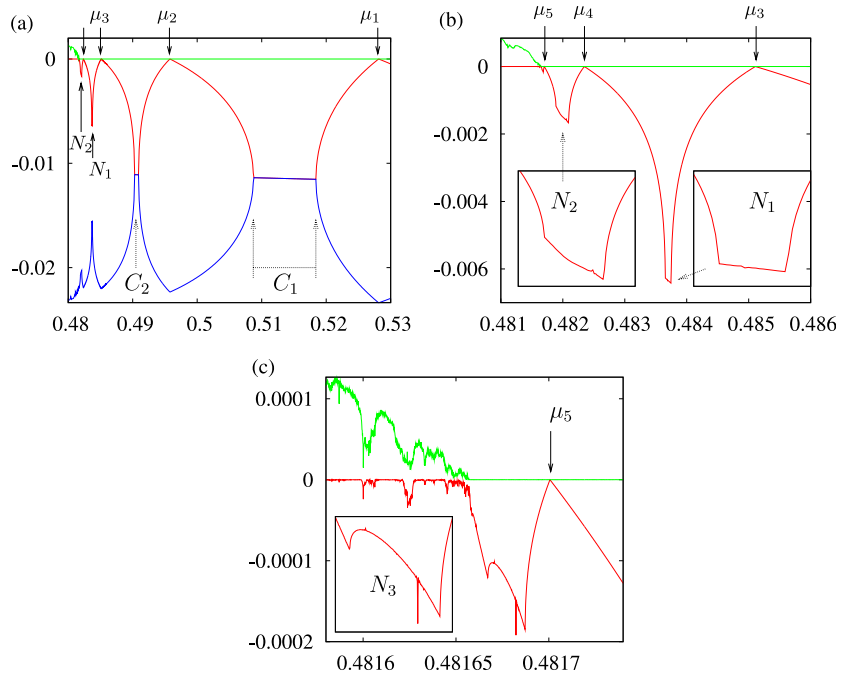

Figure 8. (a) Lyapunov exponents $\ell_1 \geqslant \ell_2 \geqslant \ell_3$ (in green, red and blue, respectively), for $\delta/(2\pi)$ fixed at 0.0324 and for a decreasing sequence of values of μ. (b),(c) Subsequent magnifications near the formation of a quasi-periodic strange attractor. Locations of quasi-periodic period doublings are labelled by 1 to 5. Normal behaviour of focus type occurs in the two parameter intervals labelled by C_1, C_2. The boxes in (b) and (c) magnify parameter regions N_1, N_2, N_3 for which the invariant circle attractors are non-reducible. N_1 and N_2 are marked by arrows in (a).

The 'side' boundaries of the resonance tongues consist of quasi-periodic saddle-node bifurcations of invariant circles: these occur on Cantor-like frayed boundaries, interspersed by resonance 'bubbles' [4, 9]. The dynamical complexity near these bifurcations has been studied by Chenciner [25–27]. The intermittency route, however, *does not depend on the resonance 'bubbles'*. Our numerical results suggest that a phase-locked invariant 2-torus is destroyed by a homo- or heteroclinic tangency inside a resonance tongue. When the two invariant circles (the attractor and the saddle) merge and disappear through a quasi-periodic saddle-node bifurcation, a strange attractor appears at once. This is similar to the second scenario described in [11, section 3.2]: there the basic object is a periodic orbit, whereas it is a quasi-periodic invariant circle in our case.

The intermittency route is now illustrated with a numerical example. The process starts with a 2-torus attractor $\mathscr{T}_-$ (figure 9(A)). As μ is decreased, a resonance tongue is approached. The dynamics on $\mathscr{T}_-$ is characterized by intermittency near the tongue boundary (figure 9(B)), due to the nearby occurrence of quasi-periodic saddle-node bifurcations (see remark 4). The 2-torus attractor $\mathscr{T}_-$ becomes phase-locked within the tongue, that is $\mathscr{T}_- = \mathscr{L}_- \cup W^u(\mathscr{L}_+)$, where $\mathscr{L}_-$ is an invariant circle attractor (figure 10(A)) and $\mathscr{L}_+$ is a saddle.

Figure 11(a) shows the ratio $\rho = \rho_1/\rho_2$ of the two rotation numbers on $\mathscr{T}_-$. The largest *plateau* of constant ρ identifies the 2 : 15 resonance tongue where the circle attractor $\mathscr{L}_-$ in figure 10(A) exists. As explained in remark 4, it is not possible to determine whether quasi-periodic saddle-node bifurcations of $\mathscr{L}_\pm$ occur *exactly* at the endpoints of the resonance plateau. Indeed, these endpoints may fall into resonance 'bubbles' for the dynamics within

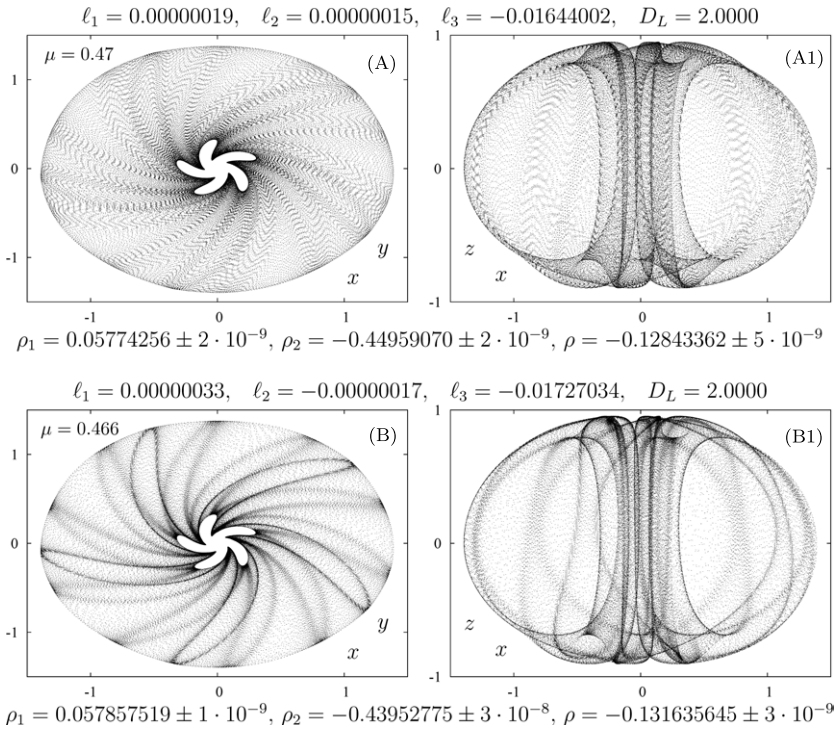

Figure 9. Quasi-periodic invariant 2-torus attractors of the diffeomorphism G (4) for $\delta/(2\pi) = 0.0247$. Top row: $\mu = 0.47$, projection on the (x, y)-plane (A) and the (x, z)-plane $(A1)$. Bottom row: $\mu = 0.466$, projection on the (x, y)-plane (B) and (x, z)-plane $(B1)$. The dynamics on these attractors is classified on the basis of numerical evidence, see remark 2. Lyapunov exponents ℓ_j and dimension D_L are given at the top of each plot. Rotation numbers ρ_j and uncertainties σ_{ρ_j}, for $j = 1, 2$ are given below each plot together with ratio $\rho = \rho_1/\rho_2$ and related uncertainty σ_ρ.

the invariant circles, see appendix A. However, the numerical evidence of figure 11 suggests that these resonances occupy parameter set of very small measure.

The ratio ρ converges with a square-root asymptotics to the value 2/15 as the resonance tongue is approached, see the magnification in the box of figure 11(a). Higher-order resonances are detected nearby, forming *secondary plateaus* of constant ρ. The 2-torus is phase-locked to an invariant circle for parameters in each plateau: there the second Lyapunov exponent ℓ_2 is negative, see the box in figure 11(c). In the 2 : 15 resonance plateau there is a parameter subinterval where the Lyapunov exponents ℓ_2 and ℓ_3 are equal (figure 11(c)). Here the invariant circle attractor $\mathscr{L}_-$ (figure 10 (A)) is of focus type.

We conjecture that the resonant 2-torus is destroyed by a homoclinic tangency of the manifolds $W^s(\mathscr{L}_+)$ and $W^u(\mathscr{L}_+)$. A strange attractor shows up at once (figure 10(B)) after $\mathscr{L}_-$ merges with $\mathscr{L}_+$ across the leftmost extreme of the resonance plateau. A slice of this attractor by a thin 'equatorial' layer displays a folded curve structure in the transversal direction (figure 12).

A regular pattern of resonance tongues persists also in the chaotic region after the breakdown of the 2-torus. Many intervals are detected where the first Lyapunov exponent ℓ_1 is zero, see figure 11(d). Computation of the rotation vector (ρ_1, ρ_2) confirms that these intervals are resonance tongues where the strange attractor is phase-locked to an invariant circle attractor (figure 11(c)). This pattern is reminiscent of the distribution of periodic windows (parameter

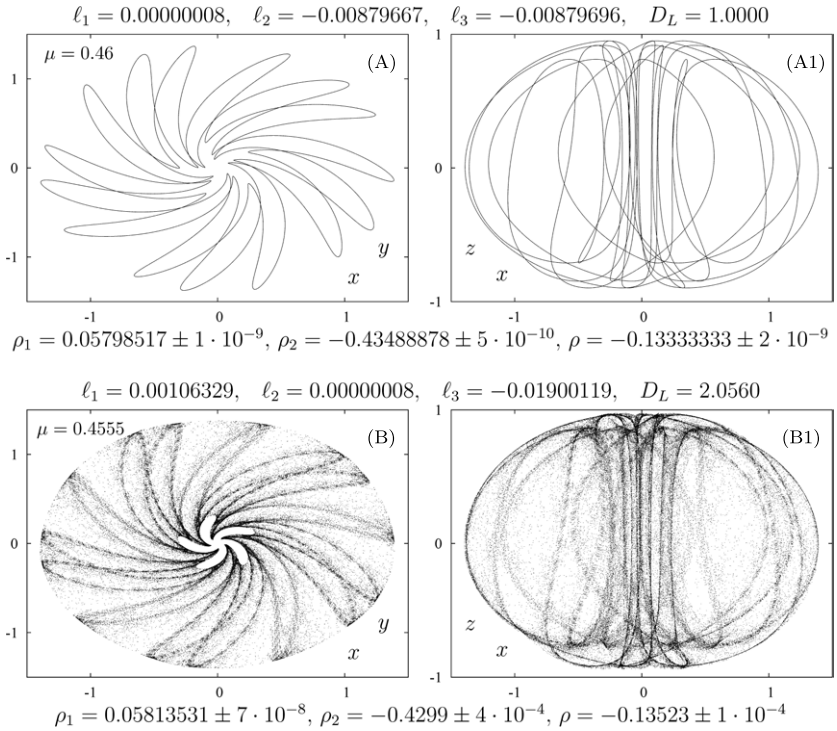

Figure 10. Attractors of the diffeomorphism G (4) for $\delta/(2\pi) = 0.0247$. Top row: quasi-periodic invariant circle attractor for $\mu = 0.46$, projection on the (x, y)-plane (A) and the (x, z)-plane $(A1)$. Bottom row: quasi-periodic Hénon-like strange attractor for $\mu = 0.4555$, projection on the (x, y)-plane (B) and (x, z)-plane $(B1)$. The dynamics on these attractors is classified on the basis of numerical evidence, see remark 2. Lyapunov exponents ℓ_j and dimension D_L are given at the top of each plot. Rotation numbers ρ_j and uncertainties σ_{ρ_j}, for $j = 1, 2$ are given below each plot together with ratio $\rho = \rho_1/\rho_2$ and related uncertainty σ_ρ.

intervals where the dynamics is characterized by sinks) amid the chaotic range in the logistic map, see, e.g., [13] for an illustration.

Remark 5: Tongue structure. There are striking analogies between the tongue structure of figure 4 and that described in [11] for the 'fattened Arnol′d map' M, defined on the cylinder $\mathbb{R} \times \mathbb{S}^1$. Map M is constructed as an approximate return map near a homoclinic tangency of a fixed point of saddle type. Heuristically speaking, the map G can be seen as a perturbation of the fattened Arnol′d map M where the role of the homoclinic tangency is played by a heteroclinic tangency of the two fixed points of saddle-focus type. A study of the relationship between the maps G and M is in preparation.

4. The heteroclinic route

For parameters on curve $\mathcal{HET}$ in figure 1, the vector field in (5) has a sphere-like heteroclinic structure formed by the union of the z-axis (which contains $W^u(P_-)$ and $W^s(P_+)$) with the 2D manifolds $W^s(P_-)$ and $W^u(P_+)$. Here $P_\pm$ are the saddle-focus fixed points located near the poles $(x, y, z) = (0, 0, \pm 1)$. The heteroclinic sphere splits into a transversal heteroclinic structure for generic families obtained by perturbing the axially symmetric 3D

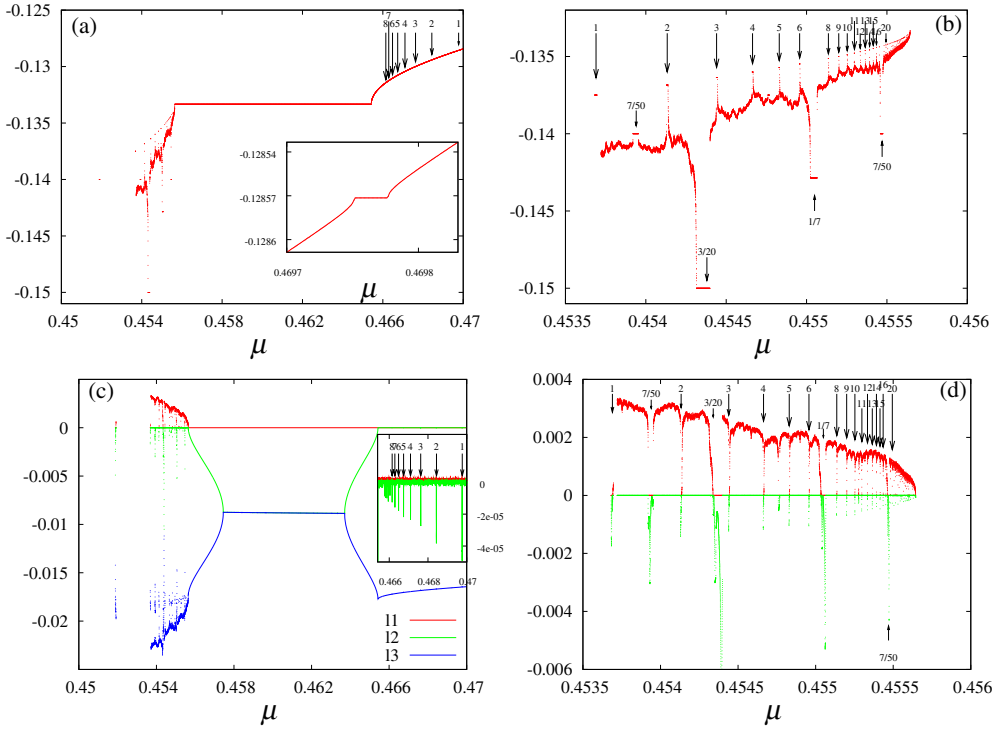

Figure 11. (*a*) Ratio $r = \rho_1/\rho_2$ of the rotation numbers of the 2-torus $\mathscr{T}_-$ as a function of μ. For μ-values where the 2-torus does not exist, the algorithm is applied to the detected attractor of G. The large plateau of constant $r = 2/15$ identifies a $2:15$ resonance tongue where $\mathscr{T}_-$ is phase-locked to a periodically invariant circle attractor. A sequence of higher-order resonances on $\mathscr{T}_-$ is marked by arrows labelled by an integer j which denotes resonance $r = (9+2*(j-1))/(70+15*(j-1))$, for $j = 1$ to 8. The rightmost resonance $j = 1$ is magnified in the box. (*b*) A regular pattern of resonance plateaus exists in the chaotic region for μ at the left of the large $2:15$ resonance plateau. The indices j denote resonances $r = (11 + 2 * (j - 1))/(80 + 15 * (j - 1))$, where j increases from 1 to 20 (with some missing values). (*c*) Lyapunov exponents $\ell_1 \geqslant \ell_2 \geqslant \ell_3$ (red, green, blue, respectively), same μ-window as (*a*). Narrow intervals where $\ell_1 = 0$ and $\ell_2 < 0$ (see the magnification in the box) correspond to the higher-order resonances labelled in (*a*). (*d*) ℓ_1 (red) and ℓ_2 (green) for the same μ-values of (*b*). Intervals where $\ell_1 = 0$ and $\ell_2 < 0$ match with the resonances identified in (*b*).

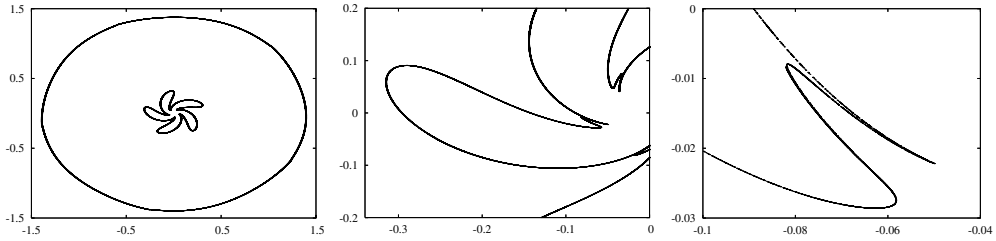

Figure 12. Left: an 'equatorial slice' of the attractor in figure 10(*B*), obtained by selecting points in a layer of width 2×10^{-5} around the plane $z = 0$, projection on the (x, y)-plane. Centre: magnification of a portion of the section. Right: further magnification. The magnifications display the local Hénon-like structure of this 'global' attractor.

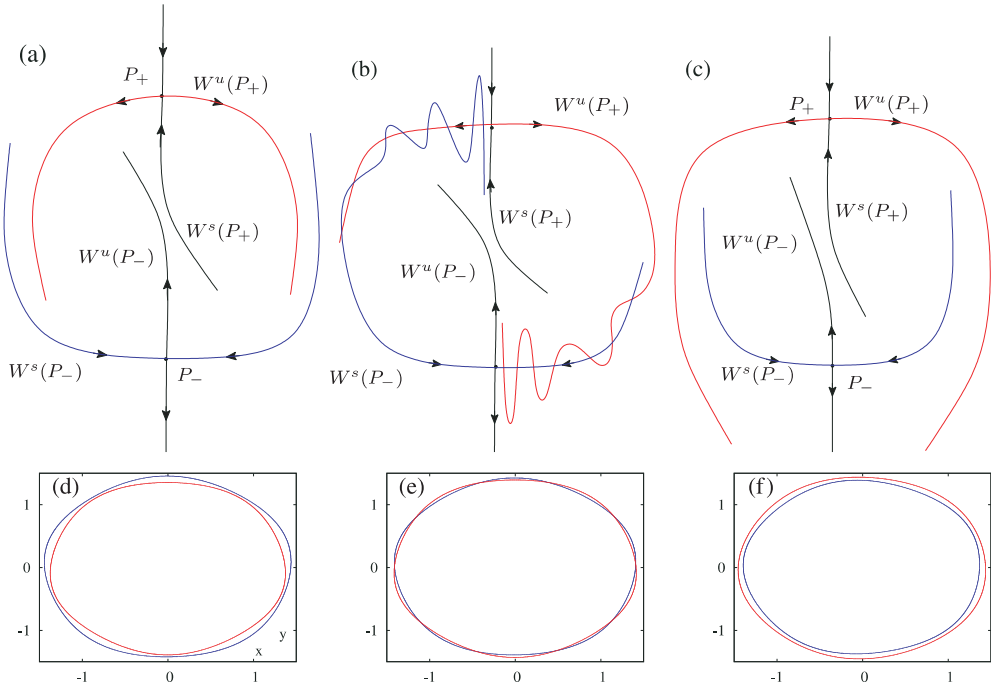

Figure 13. Top row: sketches of configurations for the invariant manifolds of the saddle-focus fixed points $P_\pm$ in region 5 (a), $\mathcal{HET}$ (b) and 4 (c), labelling as in figure 2(b). The manifolds $W^s(P_-)$ (blue) and $W^u(P_+)$ (red) are in fact two-dimensional. Bottom row: first 'equatorial' intersections of $W^s(P_-)$ (blue) and $W^u(P_+)$ (red) with the $\{z = 0\}$-plane for the map G. Here *first* means closest to P_+ or P_- in an adapted parametrization, see appendix B.3; note that $W^s(P_-)$ and $W^u(P_+)$ may fold back and have infinitely many intersections with $\{z = 0\}$. From left to right, parameters are fixed at $(\mu, \delta/(2\pi)) = (0.6, 0)$, $(0.32, 0)$ and $(0, -0.1)$.

vector field in (5), see [3, 18, 21, 39]. This allows for the occurrence of Shil′nikov homoclinic bifurcations [3, 21, 30, 31, 40, 45, 46].

Understanding the dynamics of the model map G requires a second perturbation step, this one within the class of diffeomorphisms. Additional complications arise here due to splitting of the manifolds at the tangencies. A Shil′nikov bifurcation for the vector field generically yields a wedge in parameter space for the diffeomorphism, characterized by transversal homoclinic intersections. This section aims to describe the organization of these homo/hetero-clinic phenomena in the parameter plane of the map G and their relation with the onset of strange attractors.

4.1. Heteroclinic tangencies

A perturbation argument based on phase portraits 4 and 5 in figure 1 suggests that the invariant manifolds $W^s(P_-)$ and $W^u(P_+)$ undergo the sequence of configurations sketched in figures 13(a)–(c) as μ is decreased, compare with [30, figure 5]. We recall that to decrease μ for fixed (δ, γ) roughly amounts to decrease β_2 for fixed β_1 in figure 1.

Numerical investigation shows that map G exhibits precisely this behaviour. The 2D manifold $W^u(P_+)$ is enclosed in the volume bounded by $W^u(P_-)$ for parameters at the right of I_2 in figure 3, see figure 13(d). The configuration is reversed for parameters at the left of O_2

in figures 3, see 13(f). Transversal heteroclinic intersections occur for parameters between I_2 and O_2 (figure 13(e)). By continuity, heteroclinic tangencies of $W^s(P_-)$ and $W^u(P_+)$ are expected for values of μ

(1) between those of figures 13(a) and (b): we will denote these as 'inner' tangencies;
(2) between those in figures 13(b) and (c) ('outer' tangencies).

Approximate parameter loci of these 'inner' and 'outer' heteroclinic tangencies are identified by the grey curves I_2 and O_2 in figure 3, see appendix B for the algorithm.

In summary, the 2D stable manifold $W^s(P_-)$ bounds an attracting invariant domain in phase space (figure 13(a)) for large μ. This domain is completely destroyed for small μ (figure 13 right). Indeed, no attractor is detected at the left of curve O_2 in figure 3, whereas (at least) one attractor is found at the right of I_2. For intermediate parameter values, the existence of a transversal heteroclinic structure (figure 13 centre) implies that escape to $z \to -\infty$ is possible for certain initial conditions within the concavity bounded by $W^s(P_-)$.

The heteroclinic tangencies at I_2 can be seen as a route to chaos: a strange attractor appears 'at once' when crossing certain parts of curve I_2 from left to right in figure 4. This is the case for the strange attractor in figure 14(a): its basin of attraction is bounded on the 'outside' by the 2D manifold $W^s(P_-)$, see figure 14(e). The latter panel also shows that the manifold $W^u(P_+)$ is in the basin of attraction of (a) and that $W^u(P_+)$ is very close to $W^s(P_-)$: the intersections of these manifolds with the plane $z = 0$ dist 0.00002 from each other.

A slice of the strange attractor (a) near the plane $z = 0$ shows a global Hénon-like structure winding around the origin without gaps (figure 14(c)). This strange attractor coexists with an invariant circle attractor (figure 14(b)) with a much smaller basin of attraction, see figure 14(c) and (d) for a magnification near the origin. Parameter values belong to the resonance tongue at the centre of figure 4, just at the right of curve I_2.

Remark 6: On multistability. In the region near the heteroclinic tangencies, multistability is created by the foldings produced by the splitting of separatrices (which is exponentially small in the analytic case). This cannot be detected by the normal form analysis. Indeed, in the non-resonant HSN case, the normal form (truncated to any order) coincides with the time-one map of a flow and has rotational symmetry. The only attractor is either an invariant circle or an invariant torus. If resonant terms are added to a truncated normal form, one can expect generically the occurrence of pairs of attracting and repelling invariant curves within the torus attractor, but no multistability.

The position of the separatrix $W^s(P_-)$ explains why attractors are detected for certain parameter values between the heteroclinic tangency curves I_2 and O_2 and not for others. Consider for example the finger-like tongues of figure 3, extending towards curve O_2. The attractors found for those parameter values are either invariant circles or band-like strange attractors as in figures 6(C) and (D), respectively. In those cases, the basin of attraction is 'local': it excludes a neighbourhood of the origin, see, e.g., the basin of the attractor of figure 14(b). This feature allows these attractors to 'survive' in the region between curves I_2 and O_2. In that region, the existence of attractors with a 'global' basin (as in figure 14(a)) is prevented by the transversal heteroclinic structure.

Coexistence of two strange attractors is also possible near the heteroclinic tangencies. Figure 15(b) shows a ribbon-like quasi-periodic Hénon-like strange attractor occurring at the end of a quasi-periodic doubling route (compare with figure 7($B1$)) and coexisting with the 'global' quasi-periodic Hénon-like strange attractor of panel (a). The basins of these two coexisting attractors are intertwined, see figure 15(d). The 2D manifold $W^u(P_-)$ has non-empty intersections with both basins, as shown in figure 15(e).

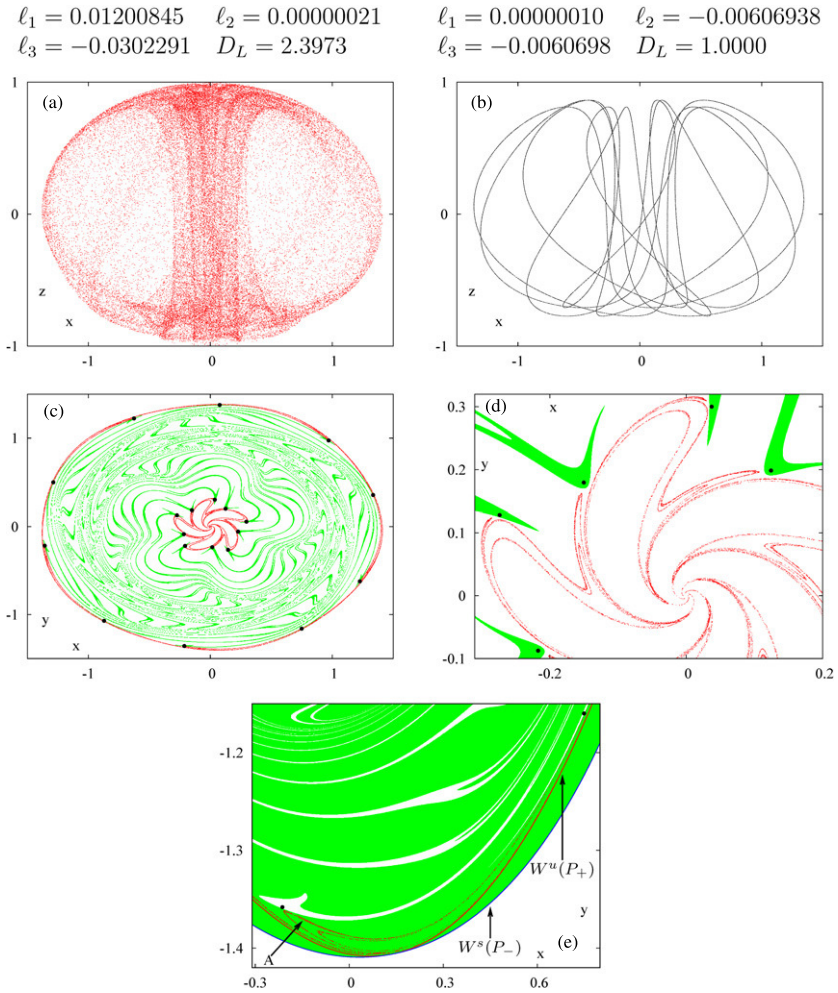

Figure 14. Coexistence of attractors of the diffeomorphism G (4) for $(\delta/2\pi, \mu) = (0.0856, 0.4784)$. (a) Quasi-periodic Hénon-like strange attractor and (b) quasi-periodic invariant circle attractor, Lyapunov exponents ℓ_j and dimension D_L are given above the panels. (c) 'Equatorial slices' of the attractors in (a) and (b) by a layer of width 2×10^{-5} around the plane $z = 0$. The slice of the attractor (a) has a similar shape to that of figure 12. The slice of the circle attractor (b) consists of 20 points (thick dots): 10 of them lie close to the outer part of the slice of (a). The intersection of the basin of (b) with the plane $z = 0$ is shown in green. (d) Magnification of (c), displaying the Hénon-like structure of the 'slice' of (a). The five thick dots belong to an 'equatorial slice' of (b). (e) Magnification of (c), displaying two thick dots in the 'equatorial slice' of (b). The intersection of the basin of (a) with $z = 0$ is shown in green. The outer edge of this basin coincides with the first equatorial intersection (see appendix B) of $W^s(P_-)$ with the plane $z = 0$ (blue). The first intersection of $W^u(P_+)$ (red) is contained in the basin of attraction of (a).

Lastly, the occurrence of a heteroclinic tangency does not necessarily imply that a strange attractor is formed. For example, in suitable parameter regions

(1) a 2-torus attractor exists at both sides of I_2;
(2) an invariant circle attractor exists at both sides of I_2;
(3) strange attractors exist at both sides of I_2.

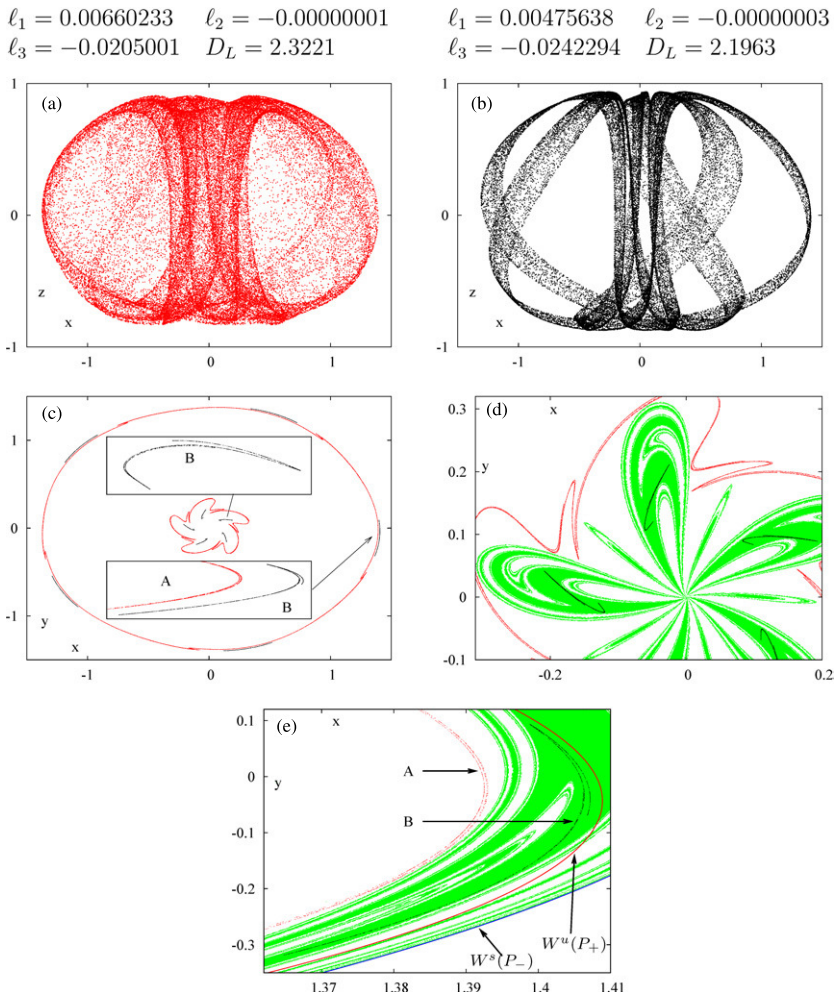

Figure 15. Coexistence of attractors of the diffeomorphism G (4) for $(\delta/2\pi, \mu) = (0.089, 0.51)$. (*a*) Quasi-periodic Hénon-like strange attractor and (*b*) ribbon-like quasi-periodic Hénon-like strange attractor, Lyapunov exponents ℓ_j and dimension D_L are given above the panels. (*c*) 'Equatorial slices' of the attractors in (*a*) and (*b*) by a layer of width 2×10^{-5} around the plane $z = 0$. The slice of the attractor (*a*) has a similar shape to that of figure 12. The slice of the attractor (*b*) consists of 5 'inner' and 5 'outer' components whose structure is strongly reminiscent of the Hénon strange attractor, see the two magnifications in the boxes. (*d*) Magnification of (*c*) near the origin, the intersection of the basin of (*b*) with $z = 0$ is shown in green. (*e*) Magnification of the lower box in (*c*), the intersection of the basin of (*b*) with $z = 0$ is shown in green. The first equatorial intersection (see appendix B) of $W^s(P_-)$ with the plane $z = 0$ (blue) bounds the union of the basins of the two attractors. The first intersection of $W^u(P_+)$ (red) has non-empty intersection with both basins of attraction.

In case 1, we have been unable to detect strange attractors near the heteroclinic tangencies: the 2D invariant manifold $W^u(P_+)$ is always attracted by the 2-torus. In case 2 we have found two possibilities: either no strange attractor is detected at the heteroclinic tangency, or a strange attractor is created and it coexists with the invariant circle attractor, see figure 14 for an example.

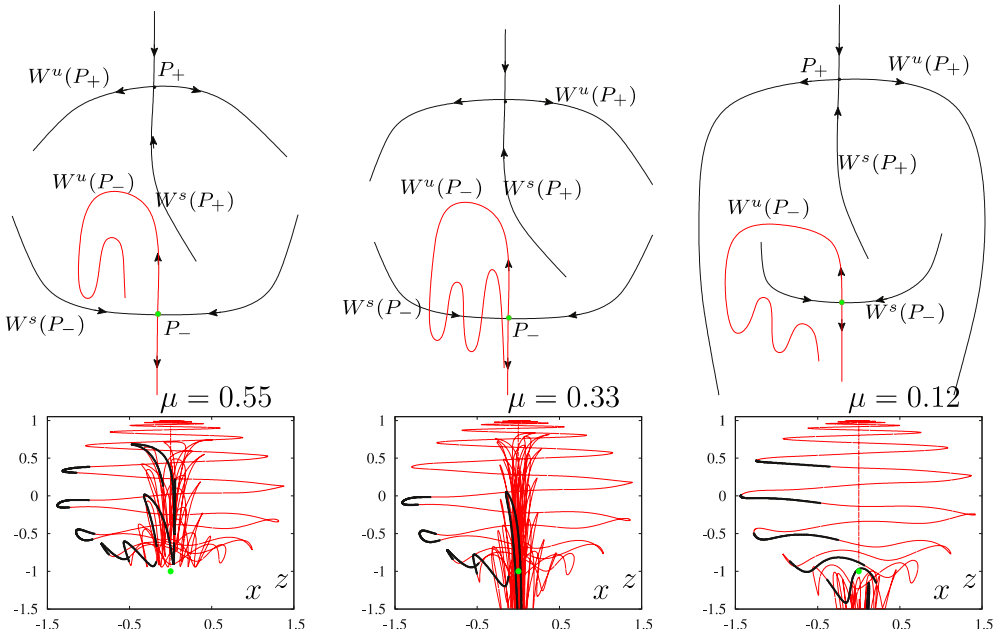

Figure 16. Top row: sketches of configurations for the invariant manifolds of the saddle-focus fixed point P_-. Bottom row: numerical examples with map G of the sketches in the top row, for $\delta = 0$ and $\mu = 0.55, 0.33, 0.12$. The fixed point P_- (green dot) is plotted with part of the 1D manifold $W^u(P_-)$ (red). A few iterations of a fundamental domain (separated by 5 iterates or multiples of 5) are plotted with thicker black lines. Note that, in fact, the manifold $W^u(P_-)$ goes up and passes very close to P_+.

4.2. Homoclinic tangencies

By construction, we expect that homoclinic tangencies occur for the saddle-focus fixed points $P_\pm$. These homoclinic tangencies can be viewed as perturbations of the Shil′nikov homoclinic bifurcations that can be expected in HSN vector fields [21, 30, 31, 40]. It is known that Hénon-like strange attractors can occur in Poincaré sections near Shil′nikov homoclinic orbits [35] of vector fields, although this result has not been formulated for unfoldings. It is therefore reasonable to expect strange attractors near homoclinic tangencies of saddle-focus fixed points of maps.

Although we have found the expected homoclinic tangencies of the 'polar' saddle foci of map G, we have been unable to detect strange attractors which are clearly identifiable as arising from those tangencies. There are indeed two problems:

(1) the homoclinic tangencies occur very close in parameter space to the heteroclinic tangencies; this is due to the closeness of the various invariant manifolds involved;
(2) as a matter of fact, we do not know what are the typical characteristics (e.g. Lyapunov dimension) of attractors arising from homoclinic tangencies of saddle-focus fixed points for 3D maps.

This section aims to illustrate point 1 above. Point 2 will be dealt in a separate study.

The perturbation argument of section 4.1, based on phase portraits 4 and 5 in figure 1, suggests the sequence of configurations illustrated in figures 16(*a*)–(*c*) as μ is decreased:

(1) $W^u(P_-)$ remains inside the hemispheric 'cup' bounded by $W^s(P_-)$;

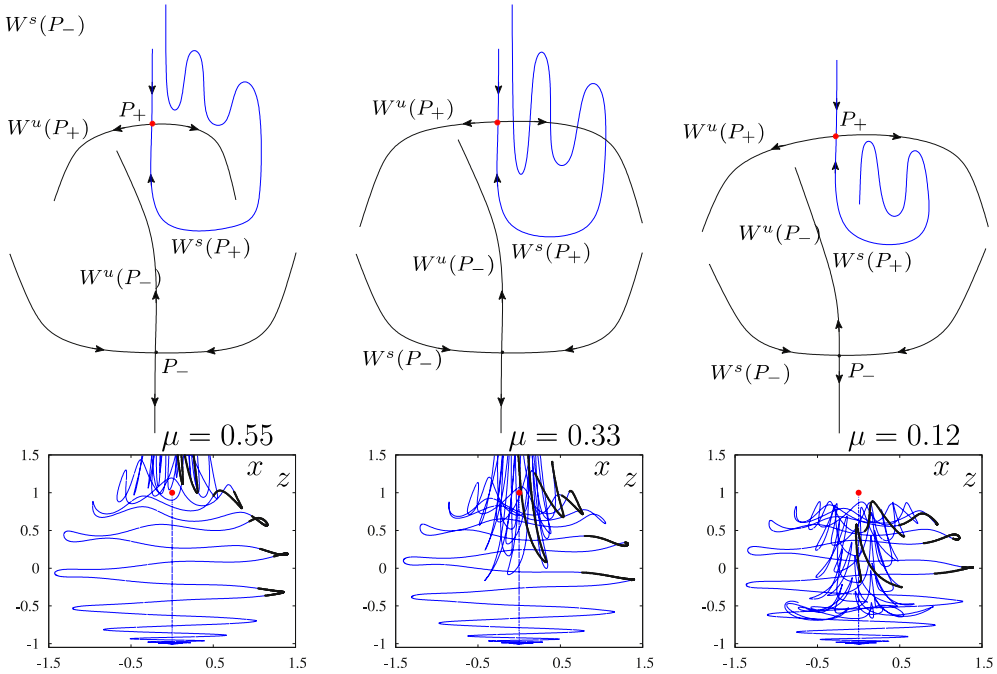

Figure 17. Top row: sketches of configurations for the invariant manifolds of the saddle-focus fixed point P_+. Bottom row: numerical examples with map G of the sketches in top row computed with map G, for $\delta = 0$ and $\mu = 0.55, 0.33, 0.12$. P_+ (red dot) is plotted with part of the 1D manifold $W^s(P_+)$ (blue) and a few iterations of a fundamental domain (separated by 5 or multiples of 5) are plotted with thicker black lines. Note that, in fact, $W^s(P_+)$ goes down until it reaches points very close to P_-.

(2) $W^u(P_-)$ has transversal homoclinic intersections with $W^s(P_-)$;
(3) $W^u(P_-)$ lies completely outside the hemispheric cup and diverges to $z \to -\infty$.

Map G exhibits this behaviour, see figures 16(d)–(f). Note that $W^u(P_-)$ passes very close to P_+, then it spirals downwards, closely following the 2D unstable manifold $W^u(P_+)$. In figure 16(d), the 1D manifold $W^u(P_-)$ 'climbs up' after its first return to U and then returns a second time to a neighbourhood of P_-. For definiteness, in what follows *we will only consider the first return of* $W^u(P_-)$ *to a neighbourhood* U *of* P_-, see appendix B.4. By continuity, (first-return) homoclinic tangencies of $W^s(P_-)$ and $W^u(P_-)$ are expected for values of μ

(1) between those of figures 16(d) and (e); we will denote these as 'inner' tangencies;
(2) between those of figures 16(e) and (f) ('outer' tangencies).

The parameter loci where the above tangencies occur will be denoted as I_{P_-} and O_{P_-}, respectively. The above discussion also holds for P_+, *mutatis mutandis*. In reversed time (that is, using the inverse G^{-1}) the downward branch of $W^s(P_+)$ first approaches P_-, then it spirals upwards closely following the 2D stable manifold $W^s(P_-)$. As μ is decreased, the expected sequence is sketched in the top row of figure 17 and the behaviour of G on the bottom row. Again, first-return homoclinic tangencies of $W^{s,u}(P_+)$ are found for values of μ:

(1) between those of figures 17(d) and (e) ('inner' tangencies);
(2) between those of figures 17(e) and (f) ('outer' tangencies).

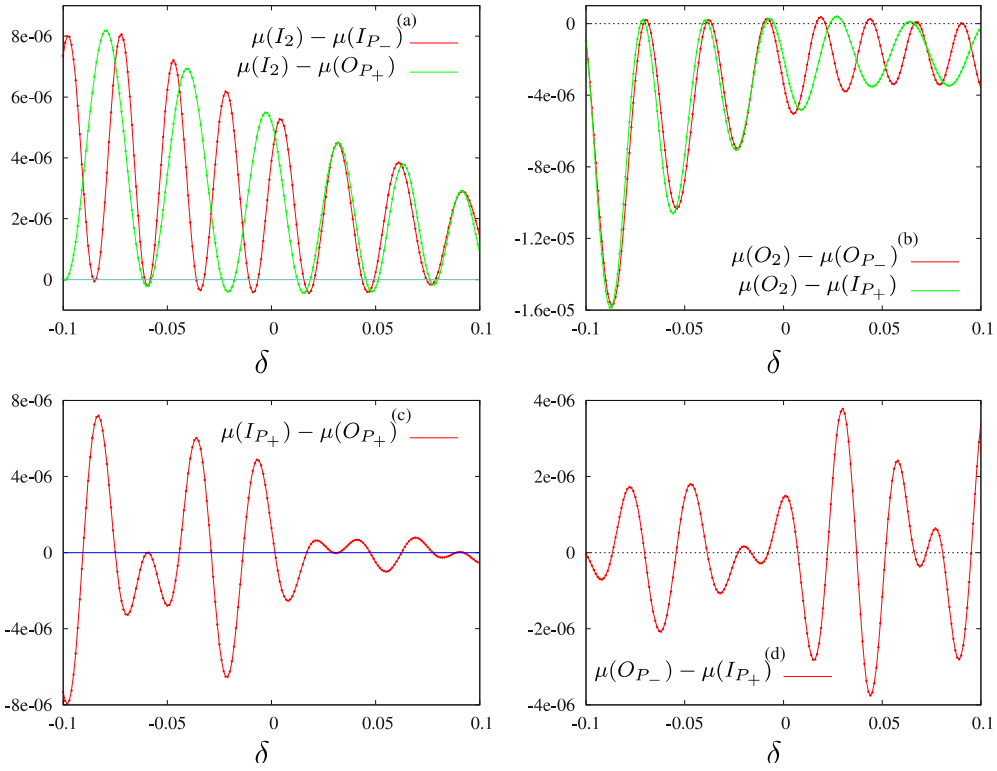

Figure 18. (*a*) Difference between the value of μ of the curves I_2 and I_{P_-} (O_{P_+}) as a function of δ, in red (green), see the text for details. (*b*) Same as (*a*) for O_2 and O_{P_-} (I_{P_+}), in red (green). (*c*) Difference between the value of μ of the curves I_{P_-} and O_{P_+}. (*d*) Same as (*c*) for O_{P_-} and I_{P_+}.

The corresponding parameter loci are denoted as I_{P_+} and O_{P_+}, see appendix B for detail on the algorithm we used to compute them.

In which order do the various tangencies occur as μ is decreased? First of all, since $W^u(P_-)$ eventually follows $W^u(P_+)$ very closely, the homoclinic tangencies at I_{P_-} occur very close (in parameter space) to the heteroclinic tangencies at I_2. For the same reason, the homoclinic tangencies at O_{P_+} also occur nearby. Indeed, the distance between I_{P_-} and O_{P_+} is smaller than 10^{-5} and their relative position changes with δ, see figure 18(*c*).

Note that the homoclinic tangencies at I_{P_-} are impossible before the heteroclinic tangencies I_2 (as μ is decreased). Indeed, the two-dimensional manifold $W^u(P_+)$ is a separatrix between the 1D manifold $W^u(P_-)$ and the 2D manifold $W^s(P_-)$, compare with figure 13(*a*). Similar considerations hold near the 'outer' heteroclinic tangency, see figures 18(*b*) and (*d*).

5. Discussion

Since we deal with the study of a diffeomorphism, an infinite amount of qualitative detail is expected to occur, which in principle may depend on the full jet of the map. However, most of these phenomena are expected to occur in tiny parameter domains. In previous and ongoing work [14, 15], we have shown that model map G displays all the basic phenomena to be expected in generic 3D HSN-families of diffeomorphisms, within the unfolding class chosen for the Poincaré-Takens normal form (5), see figure 1. This unfolding class is the dynamically

richest for HSN vector fields [31, 40]. In this paper, we have analysed dynamical phenomena (routes to chaos, multistability), some of them being described for the first time, which cannot be inferred from the analysis of the normal form. By construction, we believe that the present family of model maps displays the most relevant features for HSN diffeomorphisms.

Several phenomena detected for G require further, specific investigation.

(1) There is still not a complete theoretical explanation for the interruption of quasi-periodic doubling cascades of invariant circles, its relation with loss-of-reducibility scenarios in [32, 33] and the onset of strange attractors, see section 2; the finiteness of the cascade for quasi-periodic attractors is a distinguishing feature with respect to the well-known infinite period doubling sequence for fixed or periodic points (see, e.g., [11, 31, 47]);
(2) similarly, there is no theoretical result concerning the quasi-periodic saddle-node intermittency route described in section 3;
(3) lastly, we have not found an explanation for the lack of Shil′nikov-like attractors near the homoclinic tangencies of the saddle-focus point P_- (see section 4). We are currently investigating a model map for this type of attractors in a setting which does not involve the nearby occurrence of HSN bifurcations.

Acknowledgments

The authors are indebted to Enric Castellà, Angel Jorba and Robert Roussarie for help and suggestions and thank the respective institutions for kind hospitality. RV acknowledges kind support by the Willis Research Network (www.willisresearchnetwork.com). The research of CS has been supported by grant MTM2006-05849/Consolider (Spain).

Appendix A. Quasi-periodic bifurcations and resonance 'bubbles'

We describe the theoretical expectations for quasi-periodic bifurcations, restricting to the case of invariant circles of a diffeomorphism. A full description of quasi-periodic bifurcations would require embedding in a family of diffeomorphisms depending on at least two parameters. Loosely speaking, one of the parameters is necessary to unfold the loss of normal hyperbolicity and another parameter is required to enforce a Diophantine condition, necessary for KAM-like persistence of the invariant circles, see [4, 9, 12, 14, 15].

Consider first the case of quasi-periodic period doublings. In the standard (generic) period doubling bifurcation of fixed points, the bifurcation set generically expected in a two-dimensional parameter plane is a piecewise smooth curve. In the quasi-periodic period doubling bifurcation, the bifurcation set is 'Cantorized' in the two-dimensional parameter plane: a dense set of resonances interrupts the bifurcation boundary. This phenomenon is sketched in figure 19 for the model map G (4), considered as a family depending on (μ, δ), compare with [36, figure 1] and [9, figure 5].

An invariant circle $\mathscr{C}$ with Diophantine rotation number occurs for (μ, δ) belonging to a Cantor-like set of curves $D_1, D_2, \ldots$, called quasi-periodic 'hairs' in [12]. The circle $\mathscr{C}$ is normally hyperbolic for parameters in the union of the so-called flat discs $A_j \cup U_j$ and is attracting in A_j and unstable in U_j. A doubled invariant circle attractor exists for parameters in $U_1, U_2, U_3, \ldots$. The points of tangency of disc U_j with A_j form a frayed (Cantorized) bifurcation boundary Q. A frayed boundary consists of a Cantor set, contained inside a curve, the gaps of which are filled up with resonance bubbles. The theory does not specify the dynamics inside the resonance 'bubbles' B_k: there we expect intricate structures of bifurcations

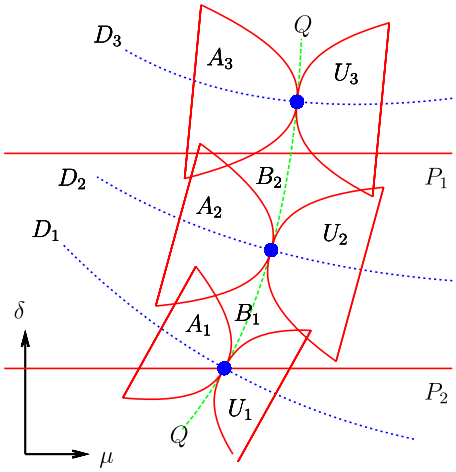

Figure 19. Sketch of the structure of the (μ, δ)-parameter plane for a quasi-periodic period doubling of an invariant circle $\mathscr{C}$ of map G (4), based on the theory of quasi-periodic bifurcations.

of periodic orbits. Subordinate quasi-periodic bifurcations are also found for the quasi-periodic Hopf bifurcation [14, 15]: a full account of these phenomena is in preparation.

Quasi-periodic period doubling bifurcations admit a simple description if the bifurcating invariant circle is reducible [33, 37, 38] and if parameters are restricted to move along a single Diophantine 'hair' D_j in the two-dimensional parameter space. In this case, one of the normal eigenvalues of the circle $\mathscr{C}$ becomes -1 at a single point along the 'hair' D_j: this is the point where the two discs A_j and U_j are tangent, see [5] and compare with the 'invariant curve theorem' of [36]. At that moment, $\mathscr{C}$ turns unstable and a doubled circle attractor $\mathscr{D}$ shows up. This may occur in two ways [22]:

(1) the circle $\mathscr{D}$ consists of a single connected curve, which is roughly twice as 'long' as the bifurcating circle $\mathscr{C}$; in this case the rotation number of $\mathscr{D}$ is halved with respect to the rotation number of the bifurcating circle $\mathscr{C}$ (near the bifurcation point) and the centre manifold of the bifurcation is a Möbius strip;
(2) the circle $\mathscr{D}$ consists of a pair of connected curves, which are mapped onto another by G (a so-called periodically invariant circle); in this case, the rotation number of G^2 is the same as the rotation number of the bifurcating circle $\mathscr{C}$ (near the bifurcation point) and the centre manifold of the bifurcation is a cylinder.

A similar discussion holds for quasi-periodic saddle-node bifurcations of invariant circles. In this case, however, the drawing of figure 19 is more involved since both the saddle and the node invariant circles occur at the same side of the frayed bifurcation boundary Q. The discussion is again simplified by fixing a Diophantine rotation number, which amounts to move along a single 'hair' in the two-dimensional parameter space.

One of the normal eigenvalues of the invariant circle becomes 1 at a single point along the 'hair' [14]. This can be viewed as the merging of two different invariant circles, a node and a saddle, with the *same (Diophantine) rotation number*. The points where this occurs form a Cantor-like frayed boundary in the two-dimensional parameter space, parametrized over the Diophantine rotation numbers [4, 9]. Chenciner [25–27] studied the phenomena occurring in the resonance 'bubbles' amidst the Cantor-like frayed boundary. The structure of 'bubbles' for quasi-periodic Hopf bifurcations was studied in [14].

In the studies of sections 2 and 3, we fix the parameter δ and only vary the parameter μ. This amounts to shift along a one-parameter path in the (μ, δ)-plane. In doing so, we cannot ensure that the chosen parameter path precisely 'hits' one of the points of the frayed bifurcation set. This would be the case for path P_2 in figure 19: such paths are called 'good paths' in [25] and correspond to a Hopf–Landau scenario, see [4, section 4.3]. We can only expect this situation with positive probability with respect to the choice of δ. Indeed, the generic case is path P_1, intersecting one of the resonance 'bubbles', since the latter are open and dense along the frayed bifurcation boundary Q (compare with, e.g., [25, figure 11]).

For the above reason, when detecting a vanishing second Lyapunov exponent (up to numerical accuracy) we can only conclude that a quasi-periodic bifurcation is expected for nearby values in the (μ, δ)-parameter plane. However, numerical evidence shows that the resonance bubbles are tiny in most of the cases: therefore, in such cases one can consider a vanishing Lyapunov exponent as a quasi-periodic bifurcation *for all practical purposes* (that is, ignoring the underlying fine-scale structure).

The above discussion is valid under the hypothesis of reducibility of the invariant circles. Reducibility means that the linearized dynamics around the invariant circle is independent on the angular coordinate along the circle in a suitable coordinate system. Following [37], consider a diffeomorphism $f : \mathbb{R}^n \to \mathbb{R}^n$ and let $x : \mathbb{S}^1 \to \mathbb{R}^n$, with $\mathbb{S}^1 = \mathbb{R}/\mathbb{Z}$, be a parametrization of an invariant circle with an irrational rotation number $\rho \in \mathbb{R}$, that is $f(\gamma(\theta)) = \gamma(\theta + \rho)$ for all $\theta \in \mathbb{S}^1$. Writing

$$f(\gamma(\theta) + h) = f(\gamma(\theta)) + D_x f(\gamma(\theta))h + O(||h||^2),$$

the linear normal behaviour around $\gamma(\theta)$ is described by the linear quasi-periodic skew-product system

$$(x, \theta) \mapsto (A(\theta)x, \theta + \rho), \tag{7}$$

where $A(\theta) = D_x f(\gamma(\theta))$ and $h \in \mathbb{R}^n$. The invariant circle parametrized by $\gamma(\theta)$ is said to be reducible if there exists a change of coordinates $x = C(\theta)y$ such that (7) becomes

$$(y, \theta) \mapsto (By, \theta + \rho), \tag{8}$$

where the matrix $B = C^{-1}(\theta)A(\theta)C(\theta)$ does not depend on θ. As it turns out, reducibility is a property of an operator on a space of functions, the so-called *transfer operator*, defined by

$$T_\rho : C(\mathbb{S}^1, \mathbb{C}^n) \to C(\mathbb{S}^1, \mathbb{C}^n), \qquad T_\rho(\phi) = \phi \circ R_\rho,$$

where $R_\rho : \mathbb{S}^1 \to \mathbb{S}^1$, $R_\rho(\theta) = \theta + \rho$ is the rigid rotation with angle ρ.

Reducibility implies that the linear stability properties of the invariant circle can be deduced by looking at the eigenvalues of the matrix B in (8). If an invariant circle is non-reducible, the full transfer operator T_ρ must be studied to determine the linear stability: this is an infinite-dimensional problem. Essentially nothing is known about quasi-periodic bifurcations in the non-reducible case, see [10, 32, 33, 38]. The skew Hopf bifurcation provides an example where KAM theory was developed for non-reducible systems [17, 24, 53, 58]. Extension of quasi-periodic bifurcation theory to non-reducible systems is a very interesting topic for future research.

Appendix B. Computational methods

Appendix B.1. One-dimensional invariant manifolds of saddle fixed points

Let p be a hyperbolic fixed point of saddle type for G such that the derivative D_pG has eigenvalues λ_j, $j = 1, 2, 3$ with $\lambda_1 \in \mathbb{R}$. Consider $\lambda_1 > 1 > |\lambda_j|$, $j = 1, 2$. The inverse

G^{-1} is used for $0 < \lambda_1 < 1 < |\lambda_j|$ and G^2 (or its inverse) for $\lambda_1 < 0$. The (local) unstable manifold of p is expressed as an adapted parametrization

$$W : \mathbb{R} \to \mathbb{R}^3, \qquad \text{with} \quad W(0) = p, \quad \text{such that} \quad G(W(t)) = W(\lambda_1 t). \tag{9}$$

The Taylor coefficients of W at the origin are computed with an algebraic manipulator up to a given order (typically 10 or 20), using the method in [48, section 10]. A fundamental domain is computed as an interval of t where the representation as a truncated Taylor series is accurate. Specifically the fundamental domain is defined as the interval $(t_0/\lambda_1, t_0)$, where t_0 is such that

$$|G(W(t)) - W(\lambda_1 t))| < \varepsilon \tag{10}$$

and ε is a user-prescribed tolerance (typically 10^{-15}). The manifold is then 'globalized' as explained in [48, section 11] (to which we refer for more details): three initial points $p_j = W(t_j)$, $j = 1, 2, 3$ are chosen with t_j in the fundamental domain. For $j = 2$ let $\Delta t_j = t_j - t_{j-1}$, $\Delta s_j = \|p_j - p_{j-1}\|$ and define $\Delta\alpha_j$ as the angle between the segments $\overline{p_j, p_{j-1}}$ and $\overline{p_{j-1}, p_{j-1}}$. A new point is computed by setting $p_{j+1} = W(t_{j+1})$, with $t_{j+1} = t_j + \Delta t_{j+1}$. If the new value t_{j+1} is larger than the upper extreme of the fundamental domain, then both t_{j+1} and Δt_{j+1} are divided by λ_1 and p_{j+1} is defined as $G(W(t_{j+1}))$: the iterate number is increased by one. This procedure is repeated, incrementing the iterate number every time that the parameter t_{j+1} exceeds t_0. If either Δs_j or $\Delta\alpha_j$ become too large (too small), then the step Δt_{j+1} is reduced. (respectively increased). The same algorithm can be used for periodic points, by replacing the map G with a suitable power of G.

Appendix B.2. Two-dimensional invariant manifolds of saddle-focus fixed points

Consider first P_+ and denote a complex eigenvalue of the derivative $D_{P_+}G$ by $\lambda = a + \mathrm{i}b$ (with $|\lambda > 1|$ and $a, b \in \mathbb{R}$). We look for an adapted parametrization, that is a function $W : \mathbb{R}^2 \to \mathbb{R}^3$ such that

$$G(W(y_1, y_2)) = W(\Lambda(y_1, y_2)), \qquad \text{where} \quad \Lambda(y_1, y_2) = \begin{pmatrix} a & -b \\ b & a \end{pmatrix} \begin{pmatrix} y_1 \\ y_2 \end{pmatrix}. \tag{11}$$

For simplicity, a linear approximation is used for $W^u(P_+)$:

$$W(y_1, y_2) = P_+ + y_1 v + y_2 \boldsymbol{u}, \tag{12}$$

where $\boldsymbol{u}, \boldsymbol{v} \in \mathbb{R}^3$ are the real and imaginary parts of an eigenvector $\boldsymbol{w} = \boldsymbol{u} + \mathrm{i}\boldsymbol{v}$ of $D_{P_+}G$ corresponding to the eigenvalue λ. Since Λ in (11) acts on $(y_1, y_2) \in \mathbb{R}^2$ as the complex multiplication λz, with $z = y_1 + \mathrm{i}y_2 \in \mathbb{C}$, a fundamental domain is an annulus in the (y_1, y_2)-coordinates. Numerically, we look for $z^0 = y_1^0 + \mathrm{i}y_1^0$ such that

$$|G(W(y_1^0, y_1^0)) - W(\lambda z^0))| < \varepsilon, \tag{13}$$

where the tolerance ε is fixed at 10^{-15}. Then a fundamental domain is the annulus bounded by the circles with centre the origin and radii $|z^0|$ and $|z^0/\lambda|$.

Appendix B.3. Heteroclinic tangencies of saddle-focus fixed points

Computation of the intersection of $W^u(P_+)$ with the plane $\{z = 0\}$ is used in section 4, see, e.g., figure 13. This is achieved with the following algorithm. An equispaced grid of points is fixed in the outer circle bounding the fundamental domain, that is the circle with centre the origin and radius $|z^0|$, see above. All points of the grid are iterated under G until the nth image of all grid points lies below the horizontal plane $\{z = 0\}$ and the $n - 1$th image lies above it. In certain cases it is necessary to slightly shift the fundamental domain, for the latter condition to be verified (this is done by reducing the modulus of z^0).

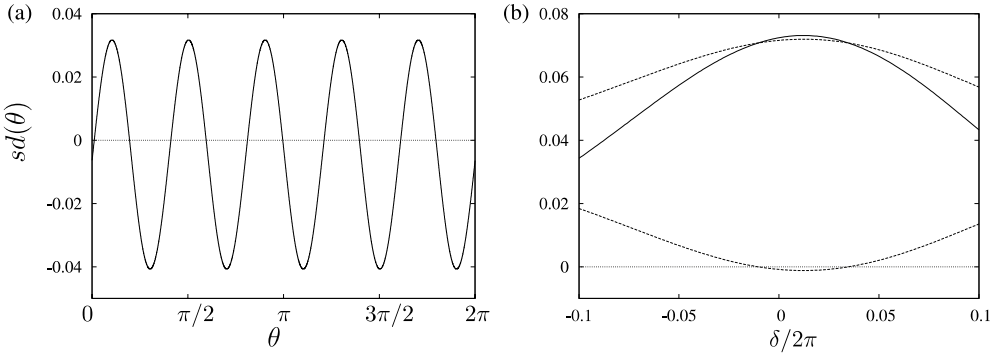

Figure 20. (*a*) Signed radial distance sd(θ) between the first 'equatorial' intersections $W^s(P_-) \cap \{z = 0\}$ and $W^u(P_+) \cap \{z = 0\}$ as a function of the angle θ defining the radial direction. Parameters $(\mu, \delta) = (0.32, 0)$ correspond to figure 13(*e*). (*b*) Amplitude (solid line), maximum and minimum (dashed lines) of the signed radial distance sd(θ) between $W^s(P_-) \cap \{z = 0\}$ and $W^u(P_+) \cap \{z = 0\}$ as a function of δ for $\mu = 0.53$. The amplitude is defined as $\max(\text{sd}(\theta)) - \min(\text{sd}(\theta))$. In an interval near $\delta = 0$ the minimum distance is negative: parameter values lie at the left of (and close to) curve I_2 in figure 3.

The intersection with $\{z = 0\}$ is computed for each point on the grid by a secant method: this yields a mesh of points in the *first* intersection of $W^u(P_+)$ with $\{z = 0\}$. Here first means closest to the origin of the adapted parametrization (see the previous section). The first intersection of $W^s(P_-)$ with $\{z = 0\}$ is computed in the same way. The curves I_2 and O_2 are 'equatorial' heteroclinic tangencies: they are computed as zeroes of the minimum signed distance sd(θ) between the first intersections of $W^u(P_+)$ and $W^s(P_-)$ with $\{z = 0\}$. The distance sd(θ) is a function sd(θ) of the angular variable θ defining the radial direction, see figure 20(*a*) for an illustration.

Generically, the point of heteroclinic tangency between $W^u(P_+)$ and $W^s(P_-)$ does not belong to the plane $\{z = 0\}$. Consequently, the curve I_2 is a *lower bound* for the location of the 'inner' heteroclinic tangencies. Indeed, 'equatorial tangencies' occurring on I_2 correspond generically to transversal heteroclinic intersections in 3D: this is observed by varying the 'height' of the horizontal intersection plane for $W^u(P_+)$ and $W^s(P_-)$. Similarly, the curve O_2 is an upper bound for the location of the 'outer' heteroclinic tangencies.

The separation between the curves I_2 and O_2 is larger near the $1:5$ gap, see figure 3. The reason is that the intersections $W^s(P_-) \cap \{z = 0\}$ and $W^u(P_+) \cap \{z = 0\}$ are more 'pentagonal' for parameters near the $1:5$ resonance gap (figure 13(f)) and 'rounder' for parameters farther from the gap (figure 13(*d*)). Consequently, the amplitude of the oscillations of sd(θ) is larger for values of μ near the $1:5$ gap, see figure 20(*b*).

Appendix B.4. Homoclinic tangencies of saddle-focus fixed points

First of all, it might be impossible to identify a 'first' tangency in the case of diffeomorphisms, compare with [11]. Indeed, if $W^u(P_-)$ is tangent to $W^s(P_-)$, then a portion of $W^u(P_-)$ will be mapped inside a tubular neighbourhood of $W^u(P_-)$, near the tangency point, by a number of iterates of the map. The returning portion of $W^u(P_-)$ may intersect $W^s(P_-)$ transversally: therefore there must have been a 'previous' tangency between $W^u(P_-)$ and $W^s(P_-)$. To remove this ambiguity, we define (unambiguously) the 'first-return' tangency as the tangency point between the *first return* of the image of a fundamental domain within

$W^u(P_-)$ to a fixed neighbourhood of P_-. Here 'first' is understood as 'closest to P_- in an adapted parametrization'.

The curves $I_{P_\pm}$ and $O_{P_\pm}$ are first-return 'inner' and 'outer' homoclinic tangencies (see section 4) and are computed as follows. Consider P_-: for fixed parameter values, a grid of points is selected inside a fundamental domain for $W^u(P_-)$ and a fixed number of iterates of G is computed for each of these points. Considering a fixed neighbourhood N of the origin, there are three possibilities, corresponding to three open regions of the parameter plane: all iterates remain inside N, all iterates escape from N, or part of the iterates escapes and part remains inside N. These three situations correspond, respectively, to figures 16(d)–(f). The first case occurs for large μ. The (μ, δ)-parameter plane is then scanned along horizontal lines (that is, for fixed δ) and by decreasing μ each time, until the configuration changes: in this way, the μ-value of the 'inner' (first-return) homoclinic tangency is *bracketed*.

A bisection procedure is then started to locate the occurrence up to a specified precision (typically, 10^{-12}). Here the more refined algorithm described at the beginning of this section is used for computation of $W^u(P_-)$. Near the first return of $W^u(P_-)$ to a neighbourhood of P_-, the images of the fundamental domain develop oscillations (figure 16 bottom row): the trick is to focus on the minimum z-values of such oscillations. Near the 'inner' homoclinic tangency, these z-minima approach P_- spiralling around it and there are two possibilities: the minima may ultimately 'climb up again' or they may fall below $W^s(P_-)$. In the former case, we are still 'before' the tangency (figure 16(d)) and in the latter case we are 'after' the tangency (figure 16(e)).

Appendix B.5. Rotation vector of an invariant 2-torus attractor for a diffeomorphism

We describe the algorithm used to compute the rotation vectors of invariant circles and 2-tori in figures 6, 9 and 11. Consider an orbit $p_j = (x_j, y_j, z_j) = G^j(x_0, y_0, z_0)$ on an invariant 2-torus attractor (see, e.g., figure 9(A)). We compute angles $\theta_j^1 = \arctan(y_j/x_j)$ and $\theta_j^2 = \arctan(z_j/r_j)$ where $r_j = \sqrt{x_j^2 + y_j^2} - c$, for some constant $c > 0$. The sequences of angles are made monotone by keeping track of how many times the angles revolve around the origin and adding a multiple of 2π accordingly.

The two rotation numbers ρ_1 and ρ_2 are estimated by a least-squares fit of the sequences $\{\theta_j^1, j = 1, \ldots, N\}$ and $\{\theta_j^2, j = 1, \ldots, N\}$ as linear functions of j, respectively. To estimate uncertainties σ_{ρ_k}, two more least square fits are performed using two different subsets of the sequences $\{\theta_j^k, j = 1, \ldots, N\}$. This yields estimates $\widehat{\rho_k}$ and $\overline{\rho_k}$ and we set $\sigma_{\rho_k} = \min\{|\widehat{\rho_k} - \rho_k|, |\overline{\rho_k} - \rho_k|\}$. The uncertainty in the ratio $\rho = \rho_1/\rho_2$ is estimated as $\sigma_\rho \approx |\rho|(\sigma_{\rho_1}/|\rho_1| + \sigma_{\rho_2}/|\rho_2|)$.

We have used 10^6 iterates of model map G along an orbit on the attractors to estimate the rotation vector. This algorithm is also applied to quasi-periodic Hénon-like strange attractors as in figure 10(B), although there is no theoretical expectation concerning the existence of a unique rotation vector in this case.

References

[1] Benedicks M and Carleson L 1991 The dynamics of the Hénon map *Ann. Math. (2)* **133** 73–169

[2] Braaksma B L J and Broer H W 1987 On a quasi-periodic Hopf bifurcation *Ann. Inst. H. Poincaré Anal. Non Linéaire* **4** 115–68

[3] Broer H W 1980 Formal normal forms for vector fields and some consequences for bifurcations in the volume preserving case *Dynamical Systems and turbulence, Warwick 1980* ed A Dold and B Eckmann (*Springer Lecture Notes in Mathematics*) vol 898 (Berlin: Springer) pp 54–74

[4] Broer H W, Huitema G B and Sevryuk M B 1996 *Quasi-periodic Motions in Families of Dynamical Systems, Order amidst Chaos* (*Springer Lecture Notes in Mathematics* vol 1645) (Berlin: Springer)

[5] Broer H W, Huitema G B, Takens F and Braaksma B L J 1990 Unfoldings and bifurcations of quasi-periodic tori *Mem. AMS* **83** 1–175

[6] Broer H W and Roussarie R 2001 Exponential confinement of chaos in the bifurcation sets of real analytic diffeomorphisms *Global analysis of Dynamical Systems: Festschrift dedicated to Floris Takens for his 60th birthday* ed H W Broer *et al* (Bristol: Institute of Physics Publishing)

[7] Broer H W, Roussarie R and Simó C 1993 On the Bogdanov–Takens bifurcation for planar diffeomorphisms *Equadiff 1991, Proc. Western European Conf. on Differential Equations* (*Barcelona, Spain 1991*) ed C Perelló *et al* (London: World Scientific) pp 81–92

[8] Broer H W, Roussarie R and Simó C 1996 Invariant circles in the Bogdanov-Takens bifurcation for diffeomorphisms *Ergod. Theory Dyn. Syst.* **16** 1147–72

[9] Broer H W and Sevryuk M B 2010 KAM Theory: quasi-periodicity in dynamical systems *Handbook of Dynamical Systems* vol 3, ed H W Broer *et al* (Amsterdam: North-Holland) at press

[10] Broer H W and Simó C 1998 Hill's equation with quasi–periodic forcing: resonance tongues, instability pockets and global phenomena *Bol. Soc. Bras. Mat.* **29** 253–93

[11] Broer H W, Simó C and Tatjer J C 1998 Towards global models near homoclinic tangencies of dissipative diffeomorphisms *Nonlinearity* **11** 667–770

[12] Broer H W, Simó C and Vitolo R 2002 Bifurcations and strange attractors in the Lorenz-84 climate model with seasonal forcing *Nonlinearity* **15** 1205–67

[13] Broer H W, Simó C and Vitolo R 2010 Chaos and quasi-periodicity in diffeomorphisms of the solid torus *Discrete Contin. Dynam. Syst. (Ser. B)* to appear, preprint available at http://people.ex.ac.uk/rv211

[14] Broer H W, Simó C and Vitolo R 2008 The Hopf-saddle-node bifurcation for fixed points of 3D-diffeomorphisms: analysis of a resonance 'bubble' *Physica* D **237** 1773–99

[15] Broer H W, Simó C and Vitolo R 2008 The Hopf-saddle-node bifurcation for fixed points of 3D-diffeomorphisms: the Arnol′d resonance web, *Bull. Bel. Math. Soc. Simon Stevin* **15** 769–87

[16] Broer H W, Simó C and Vitolo R 2005 Quasi-periodic Hénon-like attractors in the Lorenz-84 climate model with seasonal forcing *Equadiff 2003, Proc. Int. Conf. on Differential Equations (Hasselt, Belgium, 2003)* ed F Dumortier *et al* (Singapore: World Scientific) pp 714–19 ISBN 981 256 169 2

[17] Broer H W, Takens F and Wagener F O O 1999 Integrable and non-integrable deformations of the skew Hopf bifurcation *Regular Chaotic Dyn.* **4** 17–43

[18] Broer H W and Takens F 1989 Formally symmetric normal forms and genericity *Dyn. Rep.* **2** 36–60

[19] Broer H W and Takens F 2009 *Dynamical Systems and Chaos* Epsilon Uitgaven **64**

[20] Broer H W and van Strien S J 1983 Infinitely many moduli of strong stability in divergence free unfoldings of singularities of vector fields *Geometric Dynamics, Proceedings (Rio de Janeiro, 1981)* ed J Palis (*Springer Lecture Notes in Mathematics* vol 1007) pp 39–59

[21] Broer H W and Vegter G 1984 Subordinate Shil′nikov bifurcations near some singularities of vector fields having low codimension *Ergod. Theory Dyn. Syst.* **4** 509–25

[22] Broer H W and Vegter G 1992 Bifurcational aspects of parametric resonance *Dyn. Rep.* **1** 1–53

[23] Broer H W and Vitolo R 2008 Dynamical systems modeling of low-frequency variability in low-order atmospheric models *Discrete Contin. Dyn. Syst. Ser.* B **10** 401–19

[24] Broer H W and Wagener F O O 2000 Quasi-periodic stability of subfamilies of an unfolded skew Hopf bifurcation *Arch. Ration. Mech. Anal.* **152** 283–326

[25] Chenciner A 1985 Bifurcations de points fixes elliptiques. I. Courbes invariantes *Publ. Math. IHES* **61** 67–127

[26] Chenciner A 1985 Bifurcations de points fixes elliptiques. II. Orbites périodiques et ensembles de Cantor invariants *Invent. Math.* **80** 81–106

[27] Chenciner A 1987 Bifurcations de points fixes elliptiques. III. Orbites périodiques de 'petites' périodes et élimination résonante des couples de courbes invariantes *Publ. Math. IHES* **66** 5–91

[28] Ciocci M C, Litvak-Hinenzon A and Broer H W 2005 Survey on dissipative KAM theory including quasi-periodic bifurcation theory based on lectures by Henk Broer *Geometric Mechanics and Symmetry: the Peyresq Lectures* (*Lecture Notes Series* LMS306) ed J Montaldi and T Ratiu (Cambridge: Cambridge University Press) pp 303–55 ISBN-13 978-0-521-53957-9

[29] Fenichel N 1972 Persistence and smoothness of invariant manifolds for flows *Indiana Univ. Math. J.* **21** 193–226

[30] Gaspard P 1993 Local birth of homoclinic chaos *Physica* D **62** 94–122

[31] Guckenheimer J and Holmes P 1983 *Nonlinear Oscillations, Dynamical Systems, and Bifurcations of Vector Fields* (Berlin: Springer)

[32] Haro À and de la Llave R 2006 Manifolds at the verge of a hyperbolicity breakdown *Chaos* **16** 013120

[33] Haro À and de la Llave R 2007 A Parameterization method for the computation of invariant tori and their whiskers in quasi-periodic maps: explorations and mechanisms for the breakdown of hyperbolicity *SIAM J. Appl. Dyn. Syst.* **6** 142–207
[34] Hirsch M W, Pugh C C and Shub M 1977 *Invariant Manifolds* (*Springer Lecture Notes in Mathematics* vol 583) (Berlin: Springer)
[35] Homburg A J 2002 Periodic attractors, strange attractors and hyperbolic dynamics near homoclinic orbits to saddle-focus equilibria *Nonlinearity* **15** 1029–50
[36] Iooss G and Los J E 1988 Quasi-genericity of bifurcations to high-dimensional invariant tori for maps *Commun. Math. Phys.* **119** 453–500
[37] Jorba À 2001 Numerical computation of the normal behaviour of invariant curves of n-dimensional maps *Nonlinearity* **14** 943–76
[38] Jorba À and Tatjer J C 2008 A mechanism for the fractalization of invariant curves in quasi-periodically forced 1-D maps *Discrete Contin. Dyn. Syst. Ser.* B **10** 537–67
[39] Kirk V 1991 Breaking of symmetry in the saddle-node Hopf bifurcation *Phys. Lett.* A **154** 243–48
[40] Kuznetsov Yu 1998 *Elements of Applied Bifurcation Theory* 2nd edn (Berlin: Springer)
[41] Lucarini V, Speranza A and Vitolo R 2007 Parametric smoothness and self-scaling of the statistical properties of a minimal climate model: what beyond the mean field theories? *Physica* D **234** 105–23
[42] Mora L and Viana M 1993 Abundance of strange attractors, *Acta Math.* **171** 1–71
[43] Palis J and Takens F 1993 *Hyperbolicity & Sensitive Chaotic Dynamics at Homoclinic Bifurcations* (*Cambridge Studies in Advanced Mathematics* vol 35) (Cambridge: Cambridge University Press)
[44] Sánchez J, Net M and Simó C 2009 Computation of invariant tori by Newton-Krylov methods in large-scale dissipative systems *Physica* D **239** 123–33
[45] Shil′nikov L 1965 A case of existence of a countable number of periodic motions *Sov. Math. Dokl.* **6** 163–6
[46] Shil′nikov L 1970 A contribution to the problem of the structure of an extended neighborhood of a rough equilibrium state of saddle-focus type *Math. USSR—Sbornik* **10** 91–102
[47] Simó C 1979 On the Hénon–Pomeau attractor *J. Stat. Phys.* **21** 465–94
[48] Simó C 1990 On the analytical and numerical computation of invariant manifolds *Modern Methods in Celestial Mechanics* ed D Benest and C Froeschlé (Paris: Frontières) pp 285–330, also available at http://www.maia.ub.es/dsg/2004/
[49] Simó C 2005 On the use of Lyapunov exponents to detect global properties of the dynamics *Equadiff 2003, Proc. Int. Conf. on Differential Equations (Hasselt, Belgium 2003)* ed F Dumortier *et al* (Singapore: World Scientific) pp 714–19 ISBN 981 256 169 2
[50] Sterk A E, Vitolo R, Broer H W, Simó C and Dijkstra H A 2010 New nonlinear mechanisms of midlatitude low-frequency atmospheric variability *Physica* D **239** 702–18
[51] Takens F 1974 Forced oscillations and bifurcations *Applications of Global Analysis* vol 1, Communications of the Mathematical Institute Rijksuniversiteit Utrecht vol 3; reprinted in *Global analysis of dynamical systems: Festschrift dedicated to Floris Takens for his 60th birthday* ed H W Broe *et al* (Bristol: Institute of Physics Publishing)
[52] Takens F 1974 Singularities of vector fields *Publ. Math. IHES* **43** 47–100
[53] Takens F and Wagener F O O 2000 Resonances in skew and reducible quasi-periodic Hopf bifurcations *Nonlinearity* **13** 377–96
[54] Tatjer J C 2001 Three dimensional dissipative diffeomorphisms with homoclinic tangencies *Ergod. Theory Dyn. Syst.* **21** 249–302
[55] van Veen L 2005 The quasi-periodic doubling cascade in the transition to weak turbulence *Physica* D **210** 249–61
[56] Viana M 1993 Strange attractors in higher dimensions *Bol. Soc. Bras. Mat.* **24** 13–62
[57] Vitolo R 2003 Bifurcations of Attractors in 3D Diffeomorphisms *PhD Thesis* University of Groningen
[58] Wagener F O O 1998 On the skew Hopf bifurcation *PhD Thesis* University of Groningen
[59] Wang Q and Young L-S 2001 Strange attractors with one direction of instability *Commun. Math. Phys.* **218** 1–97